Received: 9 February 2024 | Revised: 31 May 2024 | Accepted: 3 July 2024

DOI: 10.1002/qj.4820

Quarterly Journal of the Royal Meteorological Society RMetS

RESEARCH ARTICLE

Increasing frequency and precipitation intensity of convective storms in the Peruvian Central Andes: Projections from convection-permitting regional climate simulations

Yongjie Huang[1] | **Ming Xue**[1,2] | **Xiao-Ming Hu**[1,2] | **Elinor Martin**[2,3] | **Héctor Mayol Novoa**[4] | **Renee A. McPherson**[3,5] | **Changhai Liu**[6] | **Mengye Chen**[1,7] | **Yang Hong**[7] | **Andres Perez**[4] | **Isaac Yanqui Morales**[4] | **José Luis Ticona Jara**[8] | **Auria Julieta Flores Luna**[4]

Correspondence
Yongjie Huang, Center for Analysis and Prediction of Storms, University of Oklahoma, Norman, OK, USA.
Email: huangynj@gmail.com; Yongjie.Huang@ou.edu

Ming Xue, Center for Analysis and Prediction of Storms; School of Meteorology, University of Oklahoma, Norman, OK, USA.
Email: mxue@ou.edu

Héctor Mayol Novoa, Universidad Nacional de San Agustín de Arequipa, Arequipa, Perú.
Email: hnovoa@unsa.edu.pe

Funding information
The Universidad Nacional de San Agustín de Arequipa (UNSA) of Peru through the IREES/LASI Global Change and Human Health Institute, Grant/Award Number: 20163646499; The U.S. Department of Energy's Atmospheric System Research, Grant/Award Number: DE-SC0024317

Abstract

To explore the potential impacts of climate change on precipitation and mesoscale convective systems (MCSs) in the Peruvian Central Andes, a region with complex terrain, two future convection-permitting regional climate simulations and one historical one are conducted using the Weather Research and Forecasting (WRF) model. All simulations adopt consistent model configurations and two nested domains with grid spacings of 15 and 3 km covering the entire South America and the Peruvian Central Andes, respectively. The historical run, spanning 2014–2019, is driven by ERA5 reanalysis, and the future simulations, covering the period 2070–2080, are driven by a bias-corrected global dataset derived from the Coupled Model Intercomparison Project Phase 6 (CMIP6) ensemble under the SSP2-4.5 and SSP5-8.5 emission scenarios. Results show geographically dependent changes in annual precipitation, with a consistent rise in the frequency of intense hourly precipitation across all regions examined. The western Amazon Basin shows a decrease in annual precipitation, while increases exist in parts of the Peruvian west coast and the east slope of the Andes under both future scenarios. In the warming scenarios, there is an overall increase in the frequency, precipitation intensity, and size of MCSs east of the Andes, with MCS precipitation volume increasing by up to ~22.2%. Despite consistently enhanced synoptic-scale low-level jets in future scenarios, changes in low-level dynamic convergence are inhomogeneous and predominantly influence annual precipitation changes. The increased convective available potential energy (CAPE), convective inhibition (CIN), and precipitable water (PW) in a warming climate suppress weak convection, while fostering a more unstable and moisture-rich atmosphere, facilitating more intense convection and the formation and intensification of heavy precipitation-producing MCSs. The study highlights the value of convection-permitting climate simulations in

For affiliations refer to page 17

projecting future severe weather hazards and informing climate adaptation strategies, especially in regions characterized by complex terrain.

KEYWORDS

convection-permitting, future projections, Peruvian Central Andes, regional climate simulations, severe convective storms

1 | INTRODUCTION

Understanding the impacts of climate change on hydroclimatic variables is vital for a wide range of sectors, including agriculture, water resources, transportation, and disaster management (IPCC, 2021). As climate change continues to impact weather systems and water cycles, having reliable future projections is crucial for mitigating risks and ensuring sustainable development (IPCC, 2022b,a; Zaitchik *et al.*, 2023). In this context, global climate models (GCMs) have been widely used to produce climate change projections under different scenarios at global and continental scales (IPCC, 2021; Juckes *et al.*, 2020; O'Neill *et al.*, 2016). However, due to constraints in computational resources, the coarse spatial resolution of current GCMs (typically at grid spacings of ~100 km, Juckes *et al.*, 2020) is a significant limitation to representing local forcings and precipitation processes (or weather conditions), particularly in regions with complex topography (Giorgi, 2019; IPCC, 2021; Kendon *et al.*, 2021).

Regional climate modeling (i.e., dynamical downscaling) offers a temporary solution to this issue, especially when using convection-permitting models (CPMs), typically at a grid spacing of 4 km or less (Giorgi, 2019; Gutierrez *et al.*, 2024; Kendon *et al.*, 2021; Lucas-Picher *et al.*, 2021; Prein *et al.*, 2015). Because CPMs have capabilities to capture local-scale forcings in greater detail, represent local and mesoscale dynamics, thermodynamics, and hydrodynamics more realistically, and resolve deep convection explicitly, their added value in simulating precipitation and mesoscale convective systems (MCSs) has been highlighted in numerous studies across various regions, including Africa (Kouadio *et al.*, 2020; Stratton *et al.*, 2018), East Asia (Guo *et al.*, 2020; Karki *et al.*, 2017; Li *et al.*, 2021; Zhu *et al.*, 2018), Europe (Berthou *et al.*, 2020; Fumière *et al.*, 2020; Lind *et al.*, 2020), North America (Liu *et al.*, 2017; Prein *et al.*, 2020; Sun *et al.*, 2016), and South America (Halladay *et al.*, 2023; Huang *et al.*, 2023a; Paccini & Stevens, 2023; Rosales *et al.*, 2022; Schumacher *et al.*, 2020). Thus, the adoption of CPMs for climate impact projections has been on the rise, particularly for examining phenomena at local and mesoscale levels (e.g., Ascott *et al.*, 2023; Gensini *et al.*, 2023; Hwang *et al.*, 2023; Ikeda *et al.*, 2021; Lind *et al.*, 2023).

Many CPM studies indicated that the frequency and intensity of hourly or sub-daily intense precipitation are projected to increase under higher greenhouse gas emission scenarios across various regions worldwide, such as Africa (Berthou *et al.*, 2019; Kendon *et al.*, 2019), East Asia (Qing & Wang, 2021), Europe (Chen *et al.*, 2021; Knist *et al.*, 2020; Lind *et al.*, 2023; Vanden Broucke *et al.*, 2019), and North America (Prein *et al.*, 2017b). For example, high-resolution CPM regional climate simulations over the United States show that, in a future climate under the Representative Concentration Pathways 8.5 (RCP8.5) scenario, strong convection is expected to increase at the expense of weak to moderate convection, supported by changes in convective available potential energy (CAPE) and convective inhibition (CIN), potentially impacting Earth's water and energy budgets (Rasmussen *et al.*, 2020). Given that MCSs are significant contributors to precipitation in many regions, including East Asia (Kukulies *et al.*, 2021; Li *et al.*, 2020), North America (Hu *et al.*, 2021), South America (Anselmo *et al.*, 2021; Paccini & Stevens, 2023; Salio *et al.*, 2007), and the Tropics (Roca & Fiolleau, 2020), understanding their behavior in CPM-based climate projections is critical to enhancing our understanding of a changing convective population and precipitation in a future climate (e.g., Fitzpatrick *et al.*, 2020; Haberlie *et al.*, 2023; Hwang *et al.*, 2023; Prein *et al.*, 2017a). Prein *et al.* (2017a) indicated that, in the CPM simulations produced by Liu *et al.* (2017), the frequency of intense summertime MCSs is projected to more than triple, and the total MCS precipitation volume is expected to increase by up to 80% in North America by the end of the century under RCP8.5. Fitzpatrick *et al.* (2020) reported that CPM simulations of Africa project a 28% increase in the extreme rain rate of MCSs by the end of the 21st century under RCP8.5, which is primarily explained by the projected increases in total column water. Hwang *et al.* (2023) conducted 4-km CPM simulations spanning 15 years for both current and future periods covering the central United States; they found significant changes in the initiation, longevity, and rain rates of warm-season MCSs under the Shared Socioeconomic Pathway 2-8.5 (SSP2-8.5) scenario, with precipitable water (PW) identified as the most crucial variable in understanding future changes. Haberlie *et al.* (2023)

examined the 3.75-km CPM simulations produced by Gensini *et al.* (2023) and found that the proportion of precipitation associated with MCSs increases significantly across the United States in both end-of-21st-century climate-change scenarios (RCP4.5 and RCP8.5).

Despite these advancements, studies of precipitation and MCSs and the associated climate change impacts using high-resolution CPM regional climate simulations remain limited in many parts of the world, such as South America, especially the Peruvian Central Andes, which is a region characterized by complex terrain and highly susceptible to the impacts of climate change (Schumacher & Rasmussen, 2020). Almazroui *et al.* (2021) analyzed the ensemble of GCMs from the Coupled Model Intercomparison Project Phase 6 (CMIP6) over South America and found that future precipitation exhibits an increase over the Peruvian Central Andes but a decrease over the Amazon Basin at the middle and end of the 21st century, and the changes are consistent across four SSPs: SSP1-2.6, SSP2-4.5, SSP3-7.0, and SSP5-8.5. Similar precipitation changes are also found in the CMIP5 multi-model ensemble mean projections under RCP 8.5, while the confidence in these projections is rather low (Pabón-Caicedo *et al.*, 2020; Sulca *et al.*, 2021). Hodnebrog *et al.* (2021) downscaled three GCMs to 50- and 10-km grid spacings covering Peru and found inconsistent precipitation trend projections as the model resolution increased. This resolution dependence suggests that CPM simulations are necessary to enhance the reliability of precipitation and MCS projections in this region, because both 50- and 10-km grid-spacing models rely strongly on the highly uncertain cumulus parameterization to produce convective precipitation. Potter *et al.* (2023) used a bias-corrected 4-km CPM simulation as the historical baseline and an ensemble of statistically downscaled CMIP5 models to reveal great increases in precipitation extremes and intensified meteorological droughts over the two most glacierized regions of Peru by the late 21st century under RCP8.5. However, uncertainties may arise from inconsistencies between the historical dynamical downscaling and the future statistical downscaling. Thus, the use of CPM climate simulations is highly desirable to produce more reliable future projections of precipitation and MCS activities in the Peruvian Central Andes region.

The primary objective of this study is to fill the noted gap by producing CPM future projections and examining projected changes in precipitation patterns and MCSs in the Peruvian Central Andes region. This research is crucial for understanding regional hydrological cycles and extreme weather events, such as flash floods, in different climate-change scenarios. Our findings will contribute to the growing body of evidence highlighting the benefits and advantages of CPMs in climate projections, especially in regions characterized by complex terrain like the Central Andes.

The remainder of the article is structured as follows: Section 2 describes the method and the datasets employed. Section 3 presents and discusses the projected changes in precipitation and MCSs. Conclusions and summary remarks are presented in Section 4.

2 | METHOD AND DATA

Both historical and future simulations in this study adopt the same model setup and physics scheme configurations as detailed in Huang *et al.* (2023a, 2023b). Specifically, the simulations use Weather Research and Forecasting (WRF) V4.2.1 (Skamarock *et al.*, 2019) with two one-way nested domains, covering the entire South America with a 15-km horizontal grid spacing (462 × 580 grid points centered at 19.678°S, 59.834°W), and the Peruvian Central Andes with a 3-km horizontal grid spacing (541 × 691 grid points centered at 14.804°S, 71.183°W), respectively. Both domains are configured with 61 stretched vertical levels, extending up to a top of 20 hPa. The physics schemes employed for both domains include a Mellor–Yamada–Nakanishi–Niino (MYNN) level 2.5 planetary boundary layer (PBL) scheme (Nakanishi & Niino, 2009), Thompson microphysics scheme (Thompson *et al.*, 2008), Unified Noah land-surface model (Ek *et al.*, 2003), revised MM5 Monin–Obukhov surface-layer scheme (Jiménez *et al.*, 2012), and Rapid Radiative Transfer Model for GCMs (RRTMG) longwave and shortwave radiation schemes (Iacono *et al.*, 2008). The Tiedtke cumulus scheme (Tiedtke, 1989) and spectral nudging are activated only in the outer domain (Huang *et al.*, 2023b). The choice of physics parameterization schemes is based on a larger number of sensitivity experiments run over a shorter period (Huang *et al.*, 2023b) and two six-year historical runs (Huang *et al.*, 2023a).

Due to computational resource constraints, two historical simulations were run using two different PBL schemes, spanning the period from 2014–2019, with the first year as the spin-up period. Huang *et al.* (2023a) show that the simulation using the MYNN PBL scheme, as described above, has a better performance in precipitation simulation, and is therefore used as the historical benchmark in this study. We refer to this historical simulation as HIST and its physics configuration is also used for future projection simulations. The initial and boundary conditions of HIST are from the hourly European Centre for Medium-Range Weather Forecasts (ECMWF) Reanalysis v5 (ERA5; Hersbach *et al.*, 2020), widely regarded as the best available reanalysis dataset. An evaluation by Huang *et al.* (2023a) indicates that HIST can successfully

reproduce the main spatiotemporal patterns of precipitation and MCSs in the Peruvian Central Andes region at both seasonal and diurnal scales, and thus demonstrates the feasibility of CPM simulations with a limited historical period for projecting potential climate-change impacts on precipitation and MCSs within the region. Huang *et al.* (2023a) also included a 4-km CPM simulation covering the entire South America produced by the South America Affinity Group (SAAG) (Dominguez *et al.*, 2024; Liu *et al.*, 2022) for comparison, and found that the primary characteristics of precipitation and MCSs are consistent within our study region across the simulations. This consistency supports the robustness of the main conclusions in this study, despite potential variations in specific values influenced by model domain size.

Two future simulations were conducted for the period 2070–2080 under two distinct SSP scenarios: SSP2-4.5 and SSP5-8.5, corresponding to the intermediate and very high greenhouse gas emission scenarios in CMIP6, respectively. The initial year (2070) serves as the spin-up period for both simulations. The two future simulations, hereinafter referred to as SSP245 and SSP585, respectively, are driven by a bias-corrected global future climate projection dataset based on the CMIP6 multi-model ensemble (Xu *et al.*, 2021). The bias-corrected global dataset is derived from 18 better CMIP6 models and *bias-corrected using the ERA5 reanalysis*, which has been shown to have a better representation of the climatology, interannual variance, and extreme events than the individual CMIP6 model projections (Xu *et al.*, 2021). This dataset has been used in several recent dynamical downscaling studies in different regions (Chang *et al.*, 2023; Wang *et al.*, 2023; Wu & Zheng, 2023; Yang *et al.*, 2023). Therefore, we utilize the ERA5 reanalysis data for the historical simulation and the best-estimated multi-model ensemble projections, bias-corrected by ERA5 reanalysis data, for future simulations. The differences between future and historical simulations should be representative across various future climate scenarios. To be consistent, time-varying concentrations of greenhouse gases, as employed in the CMIP6 Scenario Model Intercomparison Project (ScenarioMIP) for SSP2-4.5 and SSP5-8.5 scenarios (O'Neill *et al.*, 2016), were adopted in the WRF longwave and shortwave radiation schemes in the corresponding future simulations SSP245 and SSP585.

To examine changes in MCS characteristics, hourly precipitation data from both historical and future simulations are used to identify and track MCSs with an object-tracking method provided by the Python package Tracking and Object-Based Analysis of Clouds (TOBAC, Heikenfeld *et al.*, 2019), which employs a precipitation intensity threshold of 5 $mm \cdot h^{-1}$ and a minimum precipitation object area of 1000 km^2. By tracking objects, defined as spatially and temporally contiguous precipitation regions, MCS characteristics, such as precipitation intensity, size, duration, and movement speed, can be calculated. For more details on the identification and tracking of MCSs, see Huang *et al.* (2023a).

3 | RESULTS

By examining the magnitude of climate warming, the annual mean 2-m air temperature differences between SSP245 and HIST are found to be ~2.09, ~1.92, and ~2.03 °C for the mountain, foothill, and Amazon Basin regions, respectively. The corresponding differences between SSP585 and HIST are ~3.45, ~3.24, and ~3.33 °C, respectively. The following subsections will explore changes in precipitation and MCS characteristics under these warming climate scenarios.

3.1 | Changes in precipitation

In comparing annual precipitation patterns from the historical simulation (HIST) with future projections (SSP245 and SSP585: Figure 1a–c), it is evident that the SSP245 and SSP585 scenarios project a consistent trend: decreased annual precipitation over the western Amazon Basin and increased annual precipitation along the Peruvian west coast in regions below 1-km elevation, as well as in some regions on the east slope of the Andes above 1-km elevation (Figure 1d,e,g,h). These changes are generally consistent with the results of GCM projections (Almazroui *et al.*, 2021). Notably, the western Amazon Basin exhibits reductions in annual precipitation of up to 1 $mm \cdot day^{-1}$ (as shown in Figure 1d,e), corresponding to a decrease of less than 20% (Figure 1g,h) for both SSP245 and SSP585. Contrastingly, along the west coast, particularly in desert areas, the increase in annual precipitation can exceed 200%. Changes in annual precipitation within the four identified precipitation "hotspots" along the east slope of the Andes (highlighted by rectangles) are less uniform and generally not significant, characterized mostly by increased precipitation in areas above 1-km elevation and decreased precipitation below this elevation. The differences in annual precipitation between SSP245 and SSP585 are marginal across most regions (Figure 1f,i). For a clearer depiction, Figure 2 presents the area-averaged annual precipitation in six selected regions (indicated in Figure 1). Similarly, in regions 1–4 along the east slope of the Andes and region 6 on the west slope, differences between HIST and future simulations (SSP245 and SSP585) are not substantial. However, a significant reduction in annual precipitation in SSP245 and SSP585 compared with HIST is

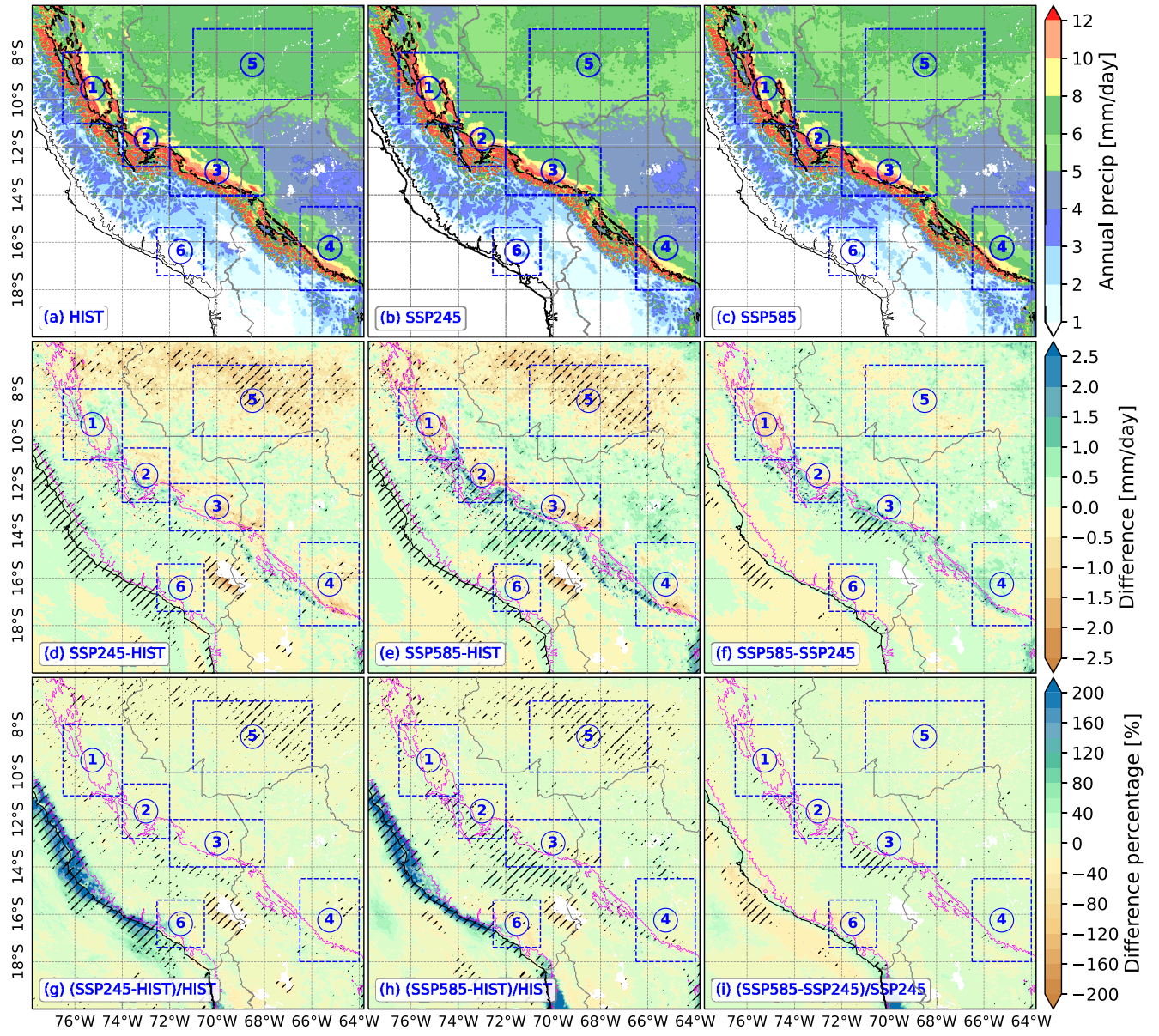

FIGURE 1 Average annual precipitation (mm·day^{-1}) in (a) HIST, (b) SSP245, and (c) SSP585. The differences in average annual precipitation (mm·day^{-1}) are presented between (d) SSP245 and HIST, (e) SSP585 and HIST, and (f) SSP585 and SSP245, and panels (g)–(i) depict their corresponding percentage difference (%). The magenta contour in each panel indicates the terrain elevation of 1 km. Areas marked with a slash pattern in (d)–(i) indicate that the differences are statistically significant at the 0.05 level. The dashed blue rectangles represent the regions used for calculating the area-averaged annual precipitation shown in Figure 2. [Colour figure can be viewed at wileyonlinelibrary.com]

observed in region 5, located over the western Amazon Basin (Figure 2). Interestingly, all six regions exhibit an increase in the standard deviation of annual precipitation in SSP245 and SSP558 relative to HIST (Figure 2), indicating an enhanced variability in annual precipitation in a warming climate. It is also noteworthy that annual precipitation is dominated by precipitation during the austral summer. The spatial patterns of changes in warm-season precipitation between the historical and future simulations are similar to those seen in annual precipitation (not shown).

To examine the sub-daily precipitation, Figure 3 displays the frequency distributions of hourly precipitation across the six regions of interest (as depicted in Figure 1) for HIST, SSP245, and SSP585. Distinct rightward shifts in precipitation intensity are witnessed when comparing the historical data (HIST) with future projections (SSP245 and SSP585: Figure 3a–f). In general, there is a clear trend of increased precipitation intensity at higher percentiles in both future simulations, indicating a potential for more frequent extreme hourly precipitation events in a warmer climate. This trend is apparent in both humid

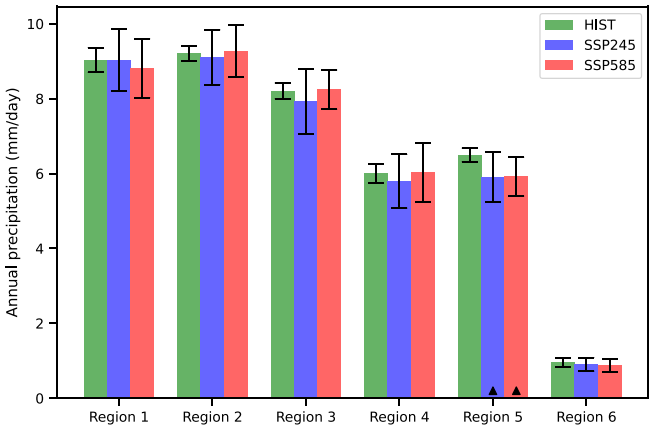

FIGURE 2 Area-averaged annual precipitation (mm·day^{-1}) for HIST (green), SSP245 (blue), and SSP585 (red) in the six regions shown in Figure 1. The error bars represent the range of ± one standard deviation. The black triangles indicate that the differences in mean annual precipitation between the historical (HIST) and future simulations (SSP245 and SSP585) are statistically significant at the 0.05 level. [Colour figure can be viewed at wileyonlinelibrary.com]

areas, such as the identified precipitation hotspots along the east slope of the Andes (regions 1–4, Figure 3a–d) and the western Amazon Basin (region 5, Figure 3e), as well as in arid zones such as region 6 (Figure 3f). At the 99.9th percentile, the precipitation intensity is notably higher in future simulations, up to a 12.1% increase in region 4 for SSP245 (Figure 3d) and up to a 16.9% increase in region 6 for SSP585 (Figure 3f), compared with HIST. These increases underscore a potential intensification of the most extreme hourly precipitation events under the SSP2-4.5 and SSP5-8.5 scenarios. Moreover, the difference between the two future scenarios becomes more pronounced with the increase of precipitation intensity, especially at the 99.9th percentile. For instance, precipitation at the 99.9th percentile in region 6 exhibits an increase of up to 10.2% when comparing SSP585 with SSP245 (as shown in Figure 3f). It suggests that the SSP5-8.5 scenario, which assumes the highest radiative forcing, could lead to a significant amplification in the frequency and intensity of extreme hourly precipitation events. Also, the analysis of the diurnal cycle of precipitation yields no significant changes in the diurnal precipitation phase and the spatial pattern of diurnal precipitation peak time. Additionally, variations in the intensity of diurnal precipitation do not display a consistent trend across the various regions or seasons (not shown). This suggests that, while other aspects of precipitation may be affected by climatic changes, the diurnal cycle of precipitation, at least in terms of peak timing and intensity, remains relatively stable. This is not surprising, as the forcing mechanisms for precipitation diurnal cycles are not expected to change much with climate warming.

Overall, changes in annual precipitation are location-dependent. Under both the SSP2-4.5 and SSP5-8.5 future scenarios, there is a general decrease in annual precipitation over the western Amazon Basin but an increase along the Peruvian west coast in areas below 1-km elevation and on the east slope of the central Andes above 1 km. Moreover, there is a consistent increase in the frequency of extreme hourly precipitation events across all regions examined, including both humid and arid regions, under the SSP2-4.5 and particularly under the SSP5-8.5 scenario compared with HIST. This suggests a consistent trend toward more frequent intense precipitation events in the future, regardless of the typical humidity levels of the regions.

3.2 | Changes in MCS characteristics

Previous studies have highlighted the significant role of MCSs in contributing to annual precipitation in the Peruvian Central Andes region (Feng *et al.*, 2021; Huang *et al.*, 2023a; Paccini & Stevens, 2023). Additionally, MCSs are frequently associated with heavy precipitation and can result in severe flooding (Schumacher & Rasmussen, 2020). In light of their critical impacts, this section focuses on examining the projected changes in the activities and properties of MCSs in the Peruvian Central Andes region.

In the historical simulation HIST, MCSs contribute over 25% of the annual precipitation and more than 30% at specific locations along the east slope of the Andes and over the western Amazon Basin (Figure 4a). This contribution is somewhat lower than the values indicated in other studies based on coarser resolution gridded precipitation products, such as the Integrated Multi-satellitE Retrievals for GPM (IMERG, at a grid spacing of 0.1 °: (e.g., Feng *et al.*, 2021)). This discrepancy can be attributed primarily to two factors: the different MCS definitions adopted in this study compared with others (e.g., also considering the area of cold cloud systems based on geostationary satellite infrared brightness temperatures, as in Feng *et al.*, 2021) and the underestimation of MCS size in CPM simulations relative to those identified in gridded precipitation products (Huang *et al.*, 2023a). A significant amount of annual precipitation results from hourly precipitation exceeding 5 mm·h^{-1} east of the Andes in CPM simulations, but these events occur in areas smaller than the precipitation area threshold of 1000 km^2 for MCS identification (not shown). Despite these differences in the specific values of MCS contributions to annual precipitation, comparative analysis of future simulations (SSP245 and SSP585) against historical data (HIST) remains a viable method to assess relative changes in MCS contributions to annual

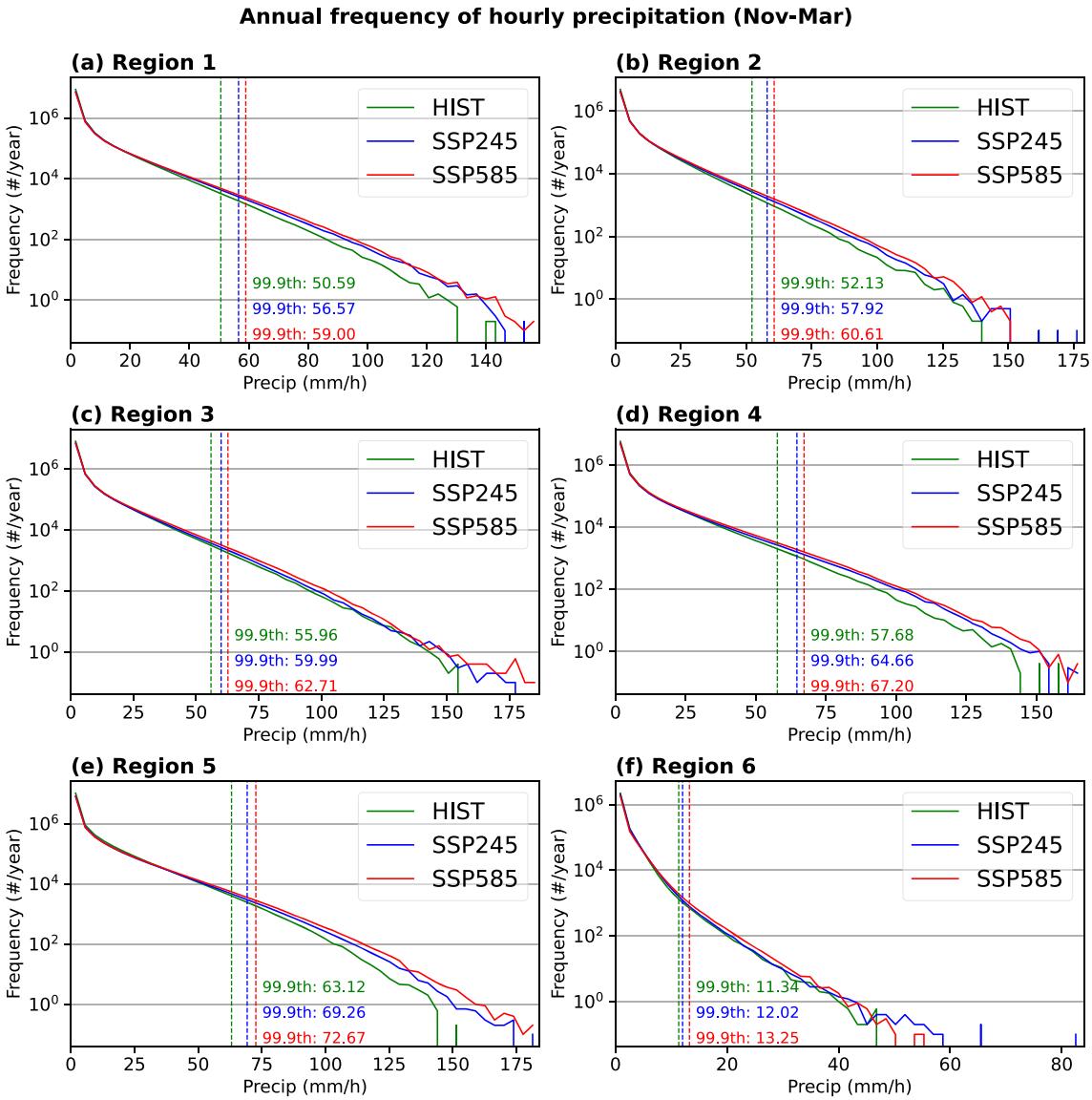

FIGURE 3 Averaged frequency (# year^{-1}) distribution of hourly precipitation (mm·h^{-1}) for HIST (green), SSP245 (blue), and SSP585 (red) in the six regions shown in Figure 1. This analysis considers only data points where hourly precipitation exceeds 0.01 mm·h^{-1} during the warm season (November–March). The Kolmogorov–Smirnov test reveals that the differences in distributions between the historical (HIST) and future simulations (SSP245 and SSP585) are statistically significant at the 0.05 level. The vertical dashed lines mark the 99.9th percentile of precipitation values (in mm·h^{-1}). [Colour figure can be viewed at wileyonlinelibrary.com]

precipitation. In SSP245 and SSP585 (Figure 4b,c), the region where the contribution of MCS precipitation to annual total precipitation exceeds 25% extends over most areas east of the Andes. Notably, areas with MCS contributions exceeding 30% expand in future simulations, with the highest contributions exceeding 40%, particularly in SSP585. Almost all areas east of the Andes within the study domain exhibit an increase in MCS precipitation contribution, with some areas experiencing increases of over 15% in both SSP245 and SSP585 (Figure 4d,e). This trend occurs despite a decrease in annual precipitation in some regions, especially over the western Amazon Basin (Figure 1d,e). Furthermore, the percentage difference in MCS precipitation contribution between the future simulations (SSP245 and SSP585) and the historical simulation (HIST) can exceed 200% along the east slope of the Andes (Figure 4g,h). Although there are no significant differences in annual precipitation between SSP245 and SSP585 (Figure 1f,i), SSP585 shows a MCS precipitation contribution up to 9% (over 20% in percentage) higher in most areas east of the Andes (Figure 4f,i).

Figure 5 displays the seasonal distribution of MCS genesis frequency in HIST, SSP245, and SSP585 as well as their differences. In HIST, the occurrence of MCSs

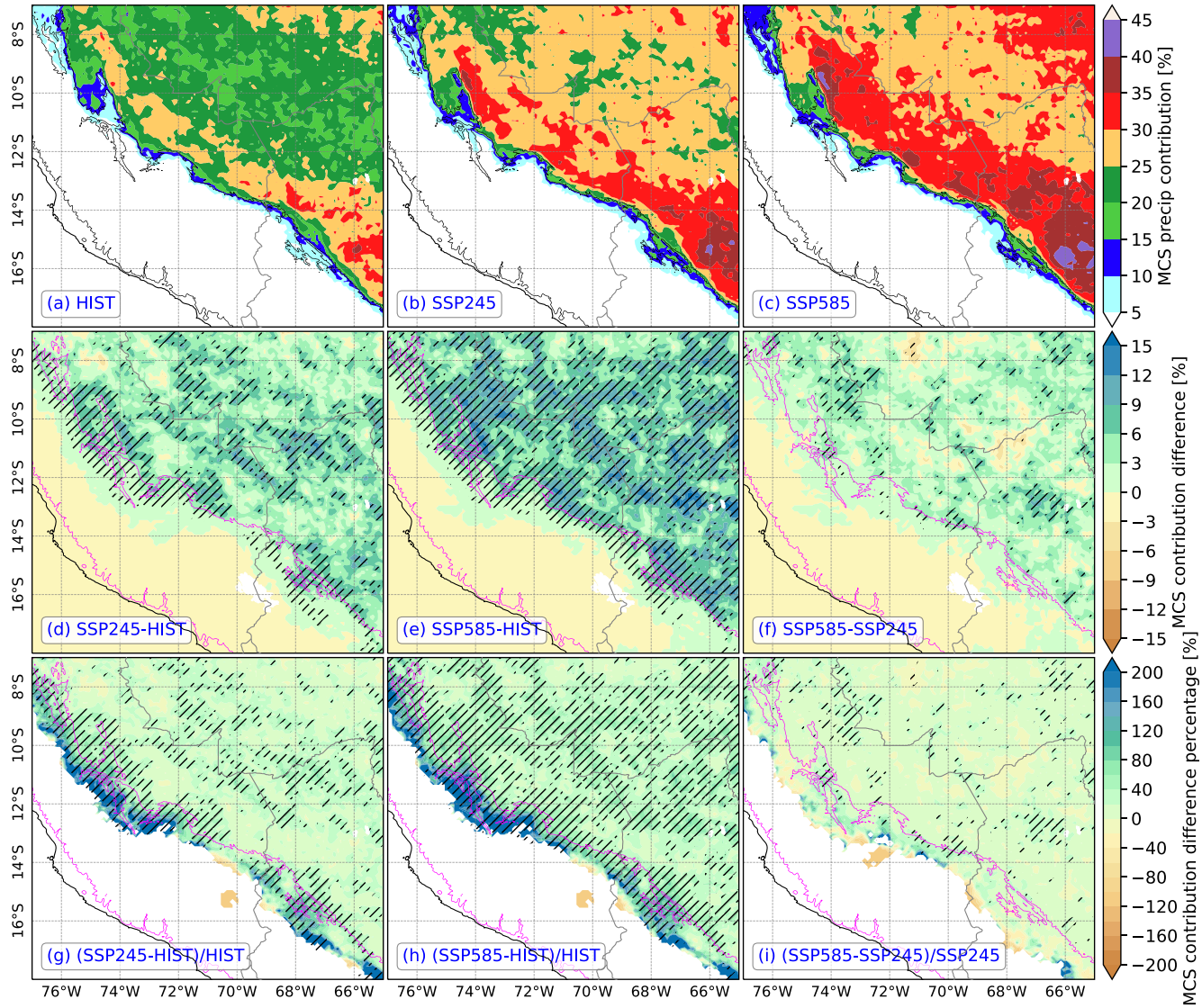

FIGURE 4 Contribution (%) of MCS precipitation to the annual precipitation for (a) HIST, (b) SSP245, and (c) SSP585. Differences in contributions are shown between (d) SSP245 and HIST, (e) SSP585 and HIST, and (f) SSP585 and SSP245. Panels (g)–(i) are percentage differences. Areas marked with a slash pattern in (d)–(i) indicate that the differences are statistically significant at the 0.05 level. The magenta contour in each panel indicates the terrain elevation of 1 km. [Colour figure can be viewed at wileyonlinelibrary.com]

is concentrated in specific regions, mainly at the precipitation hotspots along the east slope of the Andes and over the western Amazon Basin, with a higher frequency during the December–January–February (DJF) and March–April–May (MAM) seasons (Figure 5a1–a4). Compared with HIST, both SSP245 and SSP585 exhibit an overall increase in the genesis frequency of MCSs at the MCS genesis hotspots across all seasons, especially in DJF and MAM (Figure 5b1–e4). The differences in the genesis of MCSs between the future and historical simulations (SSP245 minus HIST and SSP585 minus HIST) can be up to three MCSs per season, especially along the eastern Andes in DJF and MAM (Figure 5d1–e4). The difference between SSP585 and SSP245 suggests a further increase in MCS genesis frequency under the more extreme SSP5-8.5 scenario compared with SSP2-4.5, predominantly during DJF and MAM (Figure 5f1–f4). Therefore, the results indicate a projected increase in MCS activity under future climate warming scenarios, suggesting a trend towards more frequent and intense organized storms in a warmer climate. This trend is likely to have a significant impact on regional precipitation patterns and extremes.

To examine the changes in MCS characteristics further, violin plots are employed to illustrate the distribution of key MCS properties for the historical and future simulations, including hourly mean precipitation, peak hourly precipitation, size, duration, hourly precipitation volume (hourly mean precipitation × MCS size), and movement

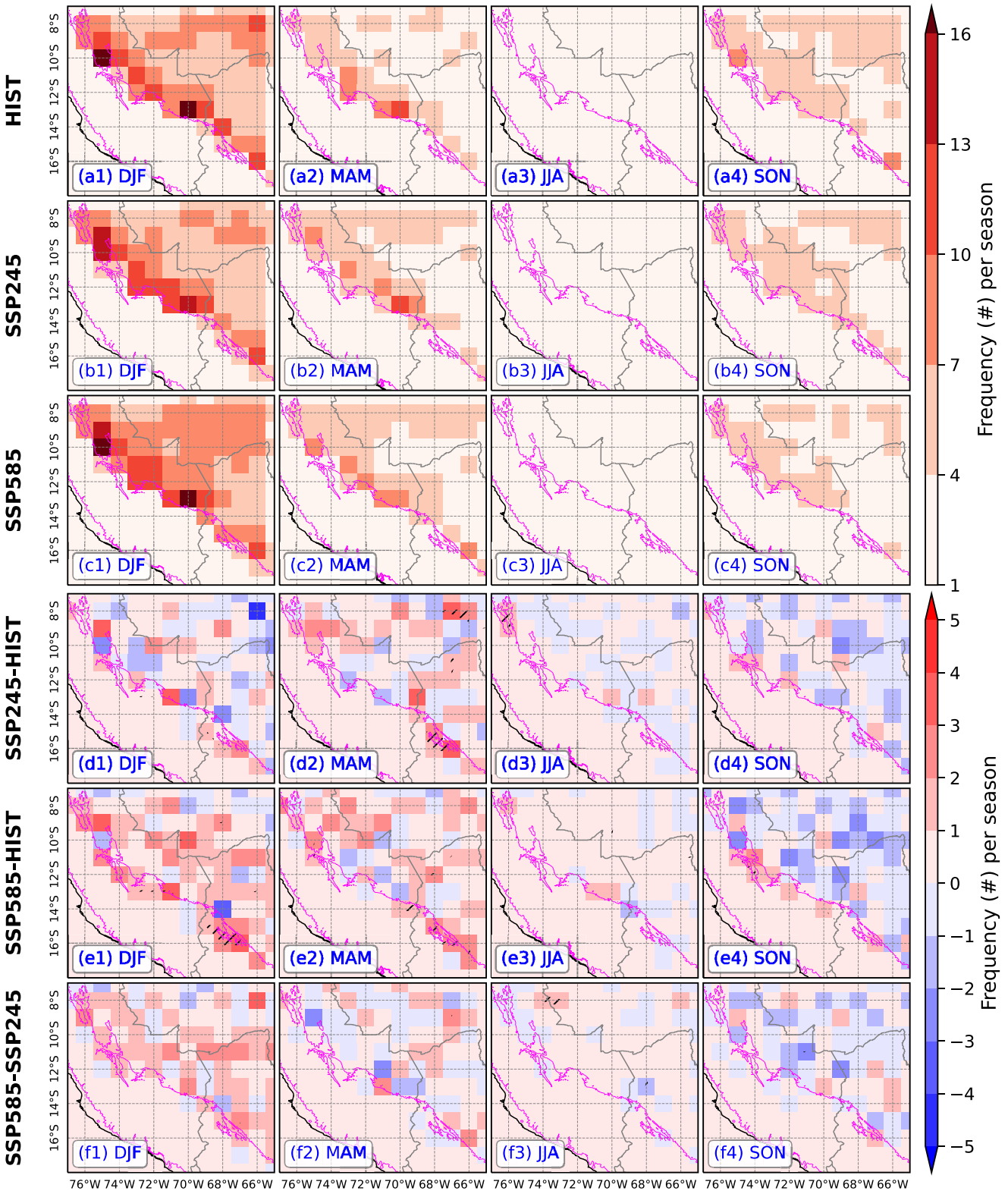

FIGURE 5 Distribution of MCS genesis frequency (counted per bin) in a 1° × 1° latitude/longitude grid in each season for (a1–a4) HIST, (b1–b4) SSP245, and (c1–c4) SSP585. Frequency differences are depicted between (d1–d4) SSP245 and HIST, (e1–e4) SSP585 and HIST, and (f1–f4) SSP585 and SSP245. (a1–f1) Summer: December–January–February (DJF), (a2–f2) autumn: March–April–May (MAM), (a3–f3) winter: June–July–August (JJA), and (a4–f4) spring: September–October–November (SON). Areas marked with a slash pattern in (d1)–(f4) indicate that the differences are statistically significant at the 0.05 level. The magenta contour in each panel indicates the terrain elevation of 1 km. [Colour figure can be viewed at wileyonlinelibrary.com]

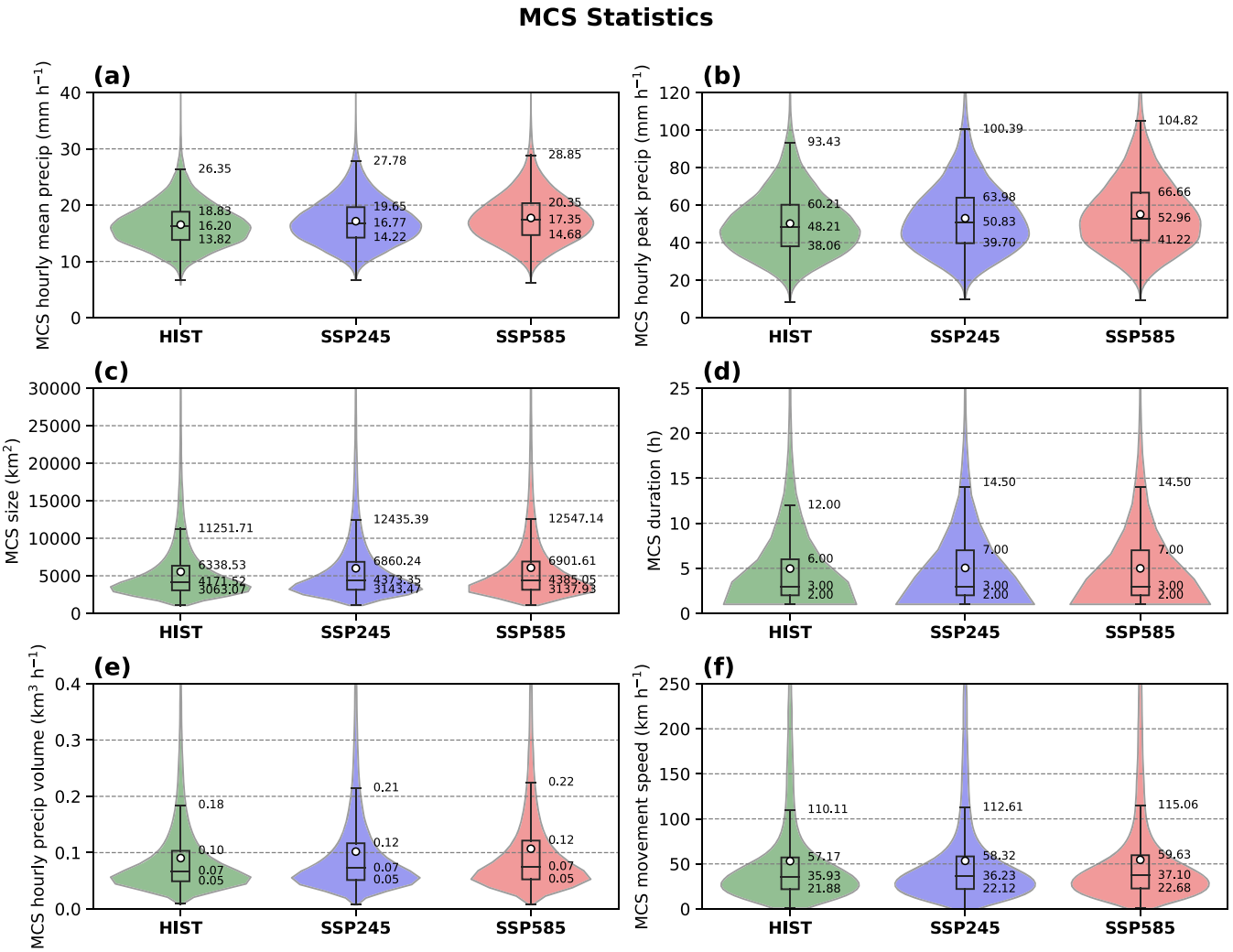

FIGURE 6 Violin plots illustrate the distribution of various MCS properties, including (a) hourly mean precipitation, (b) hourly peak precipitation, (c) size, (d) duration, (e) hourly precipitation volume, and (f) movement speed for HIST, SSP245, and SSP585. Within the accompanying box-and-whisker plots, the white circles denote the average values of the samples. Additionally, the 25th, 50th, and 75th percentiles, along with 1.5 times the interquartile range (IQR), are delineated adjacent to these plots. The distributions of HIST and the future simulations (SSP245 and SSP585) show significant differences at the 0.05 level, except for MCS duration in the comparisons of HIST with both SSP245 and SSP585, and movement speed in the comparison between HIST and SSP245. [Colour figure can be viewed at wileyonlinelibrary.com]

speed (Figure 6). For the MCS hourly mean precipitation, HIST shows a median value around 16.2 mm·h^{-1}, while SSP245 and SSP585 indicate a slight increase to ~16.8 and ~17.4 mm·h^{-1}, respectively (Figure 6a). This corresponds to an increase of ~3.7% for SSP245 and ~7.4% for SSP585. The extreme values of hourly mean precipitation, here represented by 1.5 times the interquartile range (IQR), also increase by ~5.3% in SSP245 and ~9.5% in SSP585 compared with the extreme value of ~26.4 mm·h^{-1} in HIST (Figure 6a). Peak hourly precipitation (Figure 6b) shows a more notable increase in both the median and extreme values across the simulations. The median value of peak hourly precipitation increases from 48.2 mm·h^{-1} in HIST to 50.8 mm·h^{-1} in SSP245 (an increase of ~5.4%) and 53.0 mm·h^{-1} in SSP585 (an increase of ~10.0%). Moreover, the extreme value of peak hourly precipitation rises by ~7.5% in SSP245 and ~12.2% in SSP585 compared with ~93.4 mm·h^{-1} in HIST (Figure 6b). The size of MCSs follows a similar upward trend, with median and extreme values increasing by ~4.8% and ~10.5% in SSP245, and by ~5.1% and ~11.5% in SSP585 respectively, compared with HIST (Figure 6c), suggesting MCS enlargement in future warming scenarios. Furthermore, the MCS hourly precipitation volume (Figure 6e) shows an increase in extreme values from 0.18 km^3 ·h^{-1} in HIST to 0.21 km^3 ·h^{-1} in SSP245 and 0.22 km^3 ·h^{-1} in SSP585, representing increases of about 16.7% and 22.2%, respectively. The MCS duration shows less variability across simulations,

with a median of 3 hours, and the differences in the distributions are not significant between the historical simulation and future simulations (Figure 6d). However, the extreme value of MCS duration increases from 12 hours in HIST to 14.5 hours in SSP245 and SSP585, a rise of ~20.8% (Figure 6d). It suggests that extremes in all examined MCS characteristics are projected to intensify under future warming conditions. Meanwhile, the MCS movement speed shows a slight increase in median and extreme values in SSP245 and SSP585 compared with HIST (Figure 6f). Taken together, compared with the historical simulation, the future simulations generally project an intensification of MCSs in terms of precipitation intensity and size, which could lead to amplified impacts on precipitation, flooding, and other related hazards.

3.3 | Changes in dynamic and thermodynamic conditions

The following section delves into the dynamic and thermodynamic fields to gain an understanding of the mechanisms driving the changes in precipitation patterns and MCS characteristics. Given that precipitation in the study region occurs predominantly during summer (DJF), the averaged dynamic and thermodynamic fields in DJF are examined here.

The average wind vectors at 850 hPa during DJF at four times of day show a prevailing wind direction parallel to the Andes on its eastern side, persisting throughout the day (Figure 7a1–a4). This pattern is predominantly shaped by the high, steep Andes and the South American low-level jet (SALLJ: Jones *et al.*, 2023; Marengo *et al.*, 2002, 2004; Vera *et al.*, 2006). Wind speeds display obvious diurnal variations in both slope and basin regions, as illustrated distinctly in the vertical profiles of diurnal wind speeds (Figure 8). Such variations are largely influenced by changes in the boundary-layer mixing. The wind speed decreases during the daytime due to mixing and accelerates during the night as the surface frictional effect on the boundary-layer flow fades (Figure 8). At 850 hPa, the spatial patterns of the wind field are very similar between the historical and future simulations (not shown), with the primary distinction being an increase in wind speeds, particularly in the corridor stretching from the eastern Andean foothills to the western Amazon Basin in the future simulations (Figure 7b1–b4,c1–c4). The average vertical wind profiles (Figure 8a1–c1) in the slope region show an increase in maximum wind speeds from slightly above 3.0 $m \cdot s^{-1}$ in HIST to over 4.0 $m \cdot s^{-1}$ in SSP245 and exceeding 4.5 $m \cdot s^{-1}$ in SSP585. A similar increase in wind speed is displayed in the basin region, from HIST to SSP245 and SSP585 (Figure 8a2–c2), while the maximum wind speeds in the basin region are consistently higher than those in the slope region (Figure 8). A notable characteristic of SSP245 and SSP585 is the elevation increase of the maximum wind-speed cores relative to HIST in both slope and basin regions (Figure 8). This behavior could be due to deeper mixed boundary layers under warming conditions, but is equally likely related to changes in large-scale atmospheric circulations. The small-domain CPM simulations produced in this study do not provide sufficient data to investigate variations in large-scale circulations thoroughly. This is worth investigating in the future, possibly with the help of GCM simulations.

Understanding the divergence field is crucial for comprehending the relationship between precipitation and dynamic fields. Huang *et al.* (2023a) demonstrated that precipitation and the genesis of MCSs along the east slope of the Andes are predominantly influenced by dynamic factors, particularly the low-level jet and terrain-induced uplift. In HIST, the patterns of divergence at 1000 and 1600 LST: (Local Standard Time, LST = UTC − 5 h) and convergence at 2200 and 0400 LST along the east slope of the Andes (Figure 7a1–a4) align with the diurnal precipitation variation in this region. Although the low-level jet shows an intensification in SSP245 and SSP585 (Figure 8a1–c1), the enhancement in convergence along the Andean east slope is not shown consistently (Figure 7b1–b4,c1–c4). This inconsistency is dependent on wind direction and the influence of terrain notches along the Andean east slope. Therefore, both increases and decreases in annual precipitation exist along the east slope of the Andes (Figure 1), indicating more complex relationships between dynamic processes and precipitation patterns in mountainous regions. For the western Amazon Basin region, although Huang *et al.* (2023a) indicated that the precipitation and MCS activity in this region are governed primarily by thermodynamic factors, dynamic convergence remains an essential factor for convection initiation and MCS development. From the differences in divergence fields between the future simulations and the historical simulation (Figure 7b1–b4,c1–c4), positive values (red areas) dominate the western Amazon Basin region, suggesting that convergence weakens in this region in SSP245 and SSP585 compared with HIST. This is consistent with the decrease in annual precipitation over the western Amazon Basin in both future simulations (Figure 1), underscoring the significant role of dynamic convergence alongside thermodynamic factors in influencing regional precipitation patterns. Moreover, in the comparison between SSP585 and SSP245, there is a notable escalation in the intensity of low-level jets under the more extreme SSP5-8.5 scenario (Figure 8). However, this intensification does not translate to stronger convergence at 850 hPa over the western Amazon Basin (Figure 7d1–d4).

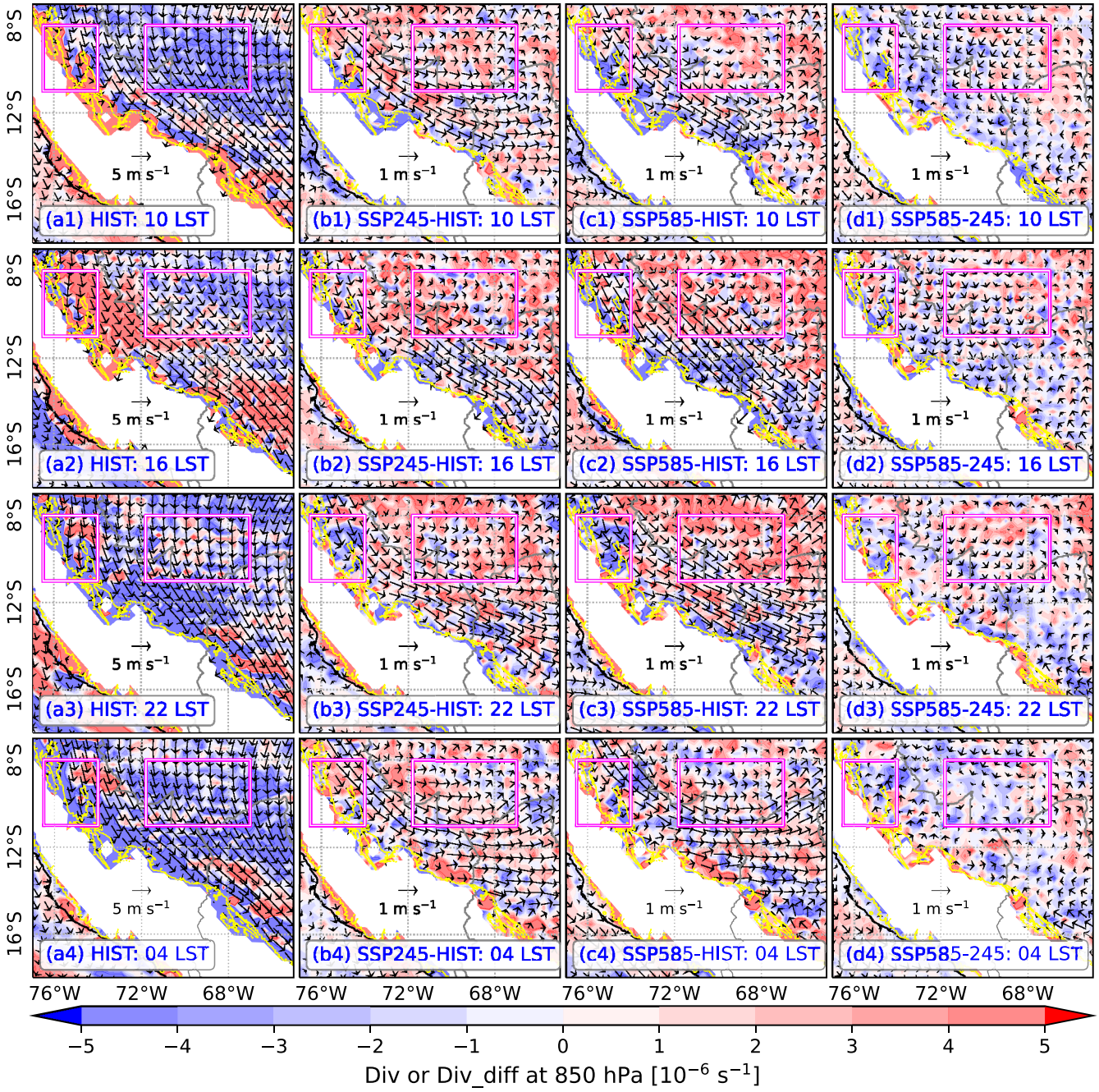

FIGURE 7 Horizontal wind vectors (m·s^{-1}) and divergence (shaded, 10^{-6} s^{-1}) at 850 hPa averaged over DJF for (a1–a4) HIST, (b1–b4) differences between SSP245 and HIST, (c1–c4) differences between SSP585 and HIST, and (d1–d4) differences between SSP585 and SSP245 at (a1–d1) 1000, (a2–d2) 1600, (a3–d3) 2200, and (a4–d4) 0400 Local Standard Time (LST = UTC − 5 h, corresponding to a longitude of 75°W), respectively. The yellow contour in each panel indicates the terrain elevation of 1 km. The magenta rectangles represent the regions used for area-averaged calculations in Figures 8 and 9. [Colour figure can be viewed at wileyonlinelibrary.com]

This lack of increased convergence aligns with the minimal differences in annual precipitation between SSP585 and SSP245 (Figure 1).

Overall, while the intensified low-level wind speeds in future warming scenarios are expected to bring more moisture from the Tropics to the Peruvian Central Andes region, and a warming climate holds more precipitable water, especially east of the Andes (not shown), it is primarily the dynamic divergence that plays a pivotal role in the changes in annual precipitation.

Large-scale dynamic divergence effectively accounts for the overall trends in annual precipitation, while it cannot explain the increased frequency of intense hourly precipitation and the heavy precipitation-producing MCSs

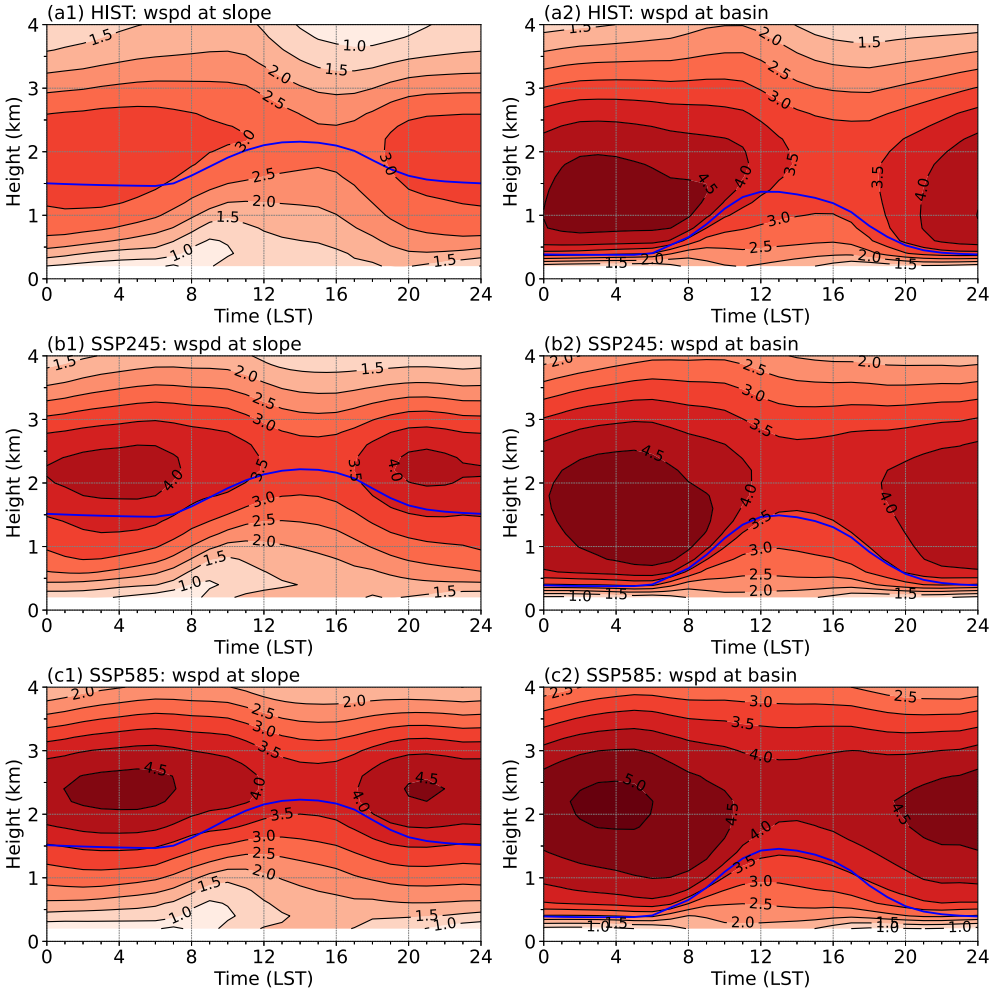

FIGURE 8 Height–time plots depict the area-averaged horizontal wind speeds ($m \cdot s^{-1}$) during DJF at MCS genesis hotspots: (a1–c1) along the eastern slope of the Andes and (a2–c2) over the western Amazon Basin (as indicated by the blue rectangles in Figure 5) in (a1,a2) HIST, (b1,b2) SSP245, and (c1,c2) SSP585. The blue curves represent the boundary-layer height (km) above the mean sea level. The *x*-axis represents the Local Standard Time (LST = UTC − 5 h), corresponding to a longitude of 75°W. [Colour figure can be viewed at wileyonlinelibrary.com]

in future simulations. This suggests that thermodynamic factors likely exert a more significant influence on the extremes of hourly precipitation. To gain a deeper insight into these influencing factors, the diurnal cycle of key thermodynamic variables is examined. This includes the CAPE, CIN, and PW in both slope and basin regions (Figure 9). Analyzing these quantities provides a further understanding of the mechanisms driving the changes in precipitation intensity and frequency in future climate scenarios.

In the slope region, CAPE shows a pronounced diurnal cycle, increasing sharply from 0700 LST to around 1300 LST, and then decreasing rapidly from 1700 LST to the early morning at 0600 LST (Figure 9a1,a2). This diurnal pattern aligns with the solar radiative heating, the nocturnal intensification of low-level jets (Figure 8a1–c1), and the diurnal precipitation cycle. There is a significant increase in CAPE at the corresponding LSTs from HIST to the future simulations, with SSP585 showing the largest increases (Figure 9a1,a2). On average, CAPE increases by ~14.6% in SSP245 and by ~28.4% in SSP585, relative to HIST. The rising CAPE suggests a more unstable atmosphere in a warming climate, which is more conducive to the development of intense convection. Compared with HIST, PW also shows an average increase of ~12.7% for SSP245 and ~21.3% for SSP585 (Figure 9a2), suggesting an enhanced moisture supply capable of fueling more intense precipitation events. However, a slight increase in CIN is also noted in the future simulations (Figure 9a1), implying a strengthened energy barrier for convection initiation, which is consistent with the decrease in weak hourly precipitation events (Figure 3) as well as more stronger convection once initiated.

In the western Amazon Basin (Figure 9b1,b2), CAPE begins to increase at 0700 LST in response to solar heating, peaks swiftly at 1100 LST, and then diminishes, presumably because of convective stabilization, corresponding to the typical pattern of afternoon precipitation development in this region (Huang *et al.*, 2023a). Increases in CAPE from HIST to SSP245 and SSP585 in the basin region (Figure 9b1) are greater in absolute magnitude but of similar percentages to those in the slope region, averaging about 17.8% and 27.5%, respectively. Meanwhile, PW in the basin region (Figure 9b2) has an increase of ~11.1%

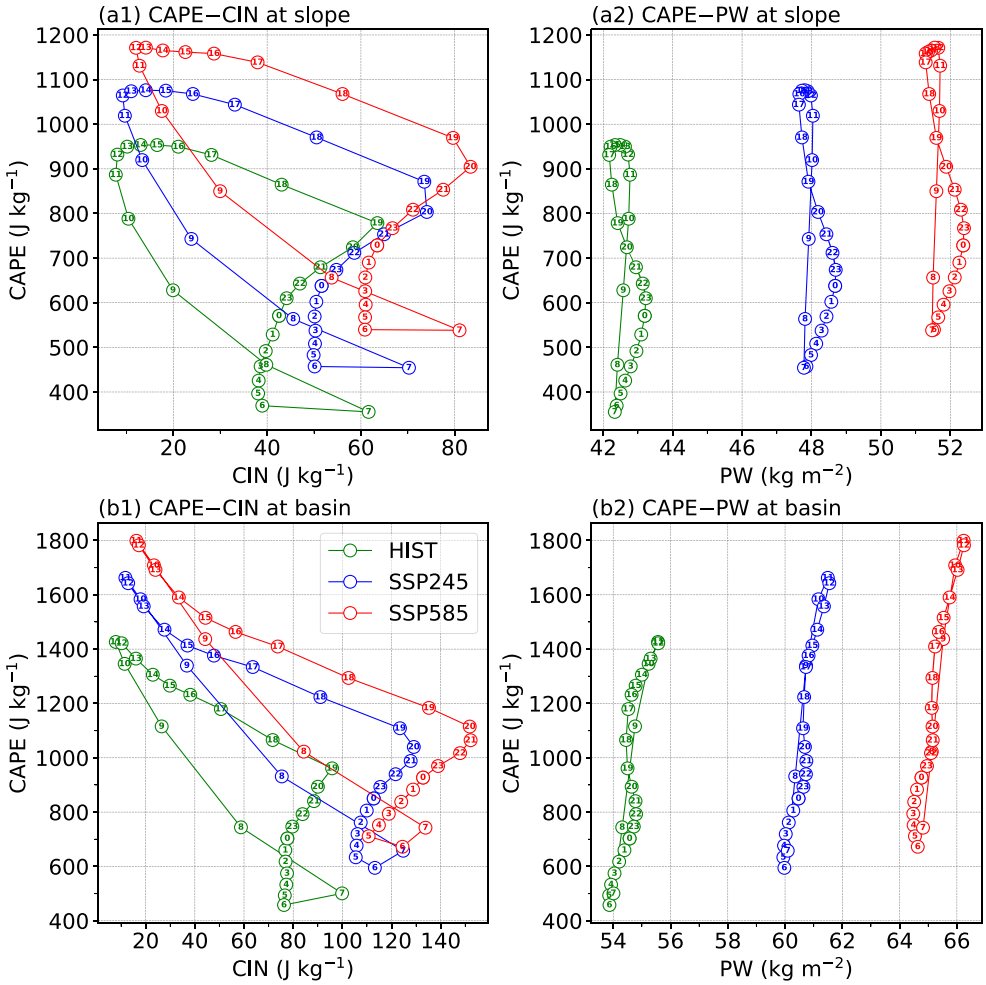

FIGURE 9 Diurnal cycle of (a1,b1) convective available potential energy (CAPE, in J·kg^{-1}) as a function of convective inhibition (CIN, in J·kg^{-1}) and (a2,b2) CAPE as a function of precipitable water (PW, in kg·m^{-2}) during DJF at MCS genesis hotspots (a1,b1) along the eastern slope of the Andes and (b1,b2) over the western Amazon Basin (as indicated by the blue rectangles in Figure 5). The numbers within the circles represent the Local Standard Time (LST = UTC − 5 h), corresponding to a longitude of 75°W. [Colour figure can be viewed at wileyonlinelibrary.com]

in SSP245 and ~19.4% in SSP585 compared with HIST. A similar increase is also found in CIN in the future simulations compared with HIST (Figure 9b1), implying an enhanced suppression of convective initiation in a warming climate.

The probability density functions (PDFs) of CAPE, CIN, and 0–6 km bulk wind shear for both the eastern slope of the Andes and the western Amazon Basin region (Figure 10) are examined to elucidate further the changes in environmental conditions under different climate scenarios. The distributions of CAPE and CIN show systematic rightward shifts for SSP245 and SSP585 compared with HIST in both slope and basin regions (Figure 10a1–b2). This indicates a higher frequency of large CAPE and CIN values and a lower frequency of small CAPE and CIN values in SSP245 and SSP585. Notably, there is an increase of ~12.8% and ~23.1% in the 90th percentile CAPE values from HIST to SSP245 and SSP585 in the slope region (Figure 10a1), and a corresponding increase of ~16.6% and ~29.5% in the basin region (Figure 10a2), indicating enhanced atmospheric instability conducive to intense convection in future climate scenarios. Since moisture is predominantly concentrated in the lower levels of the atmosphere, PW, especially its change, primarily reflects the amount and change in moisture content at the lower levels. Furthermore, increasing CAPE can induce stronger updrafts. When the increased CAPE is combined with higher PW (Figure 9), it results in a stronger upward moisture flux and increased water-vapor condensation, which is conducive to a higher precipitation rate (Prein *et al.*, 2017a). For the 90th percentile CIN values (Figure 10b1,b2), they increase by ~20.1% and ~40.6% in the slope region and by ~26.0% and 40.2% in the basin region from HIST to SSP245 and SSP585, respectively. This suggests a stronger energy barrier for convection initiation in future warming scenarios, consistent with the projected decrease in weak precipitation events and an increase in the intensity of convective storms once initiated.

Vertical wind shear is crucial for the organization and longevity of MCSs (e.g., Huang *et al.*, 2019a;Rotunno *et al.*, 1988; Schumacher & Rasmussen, 2020), with greater wind shear generally promoting the formation of more

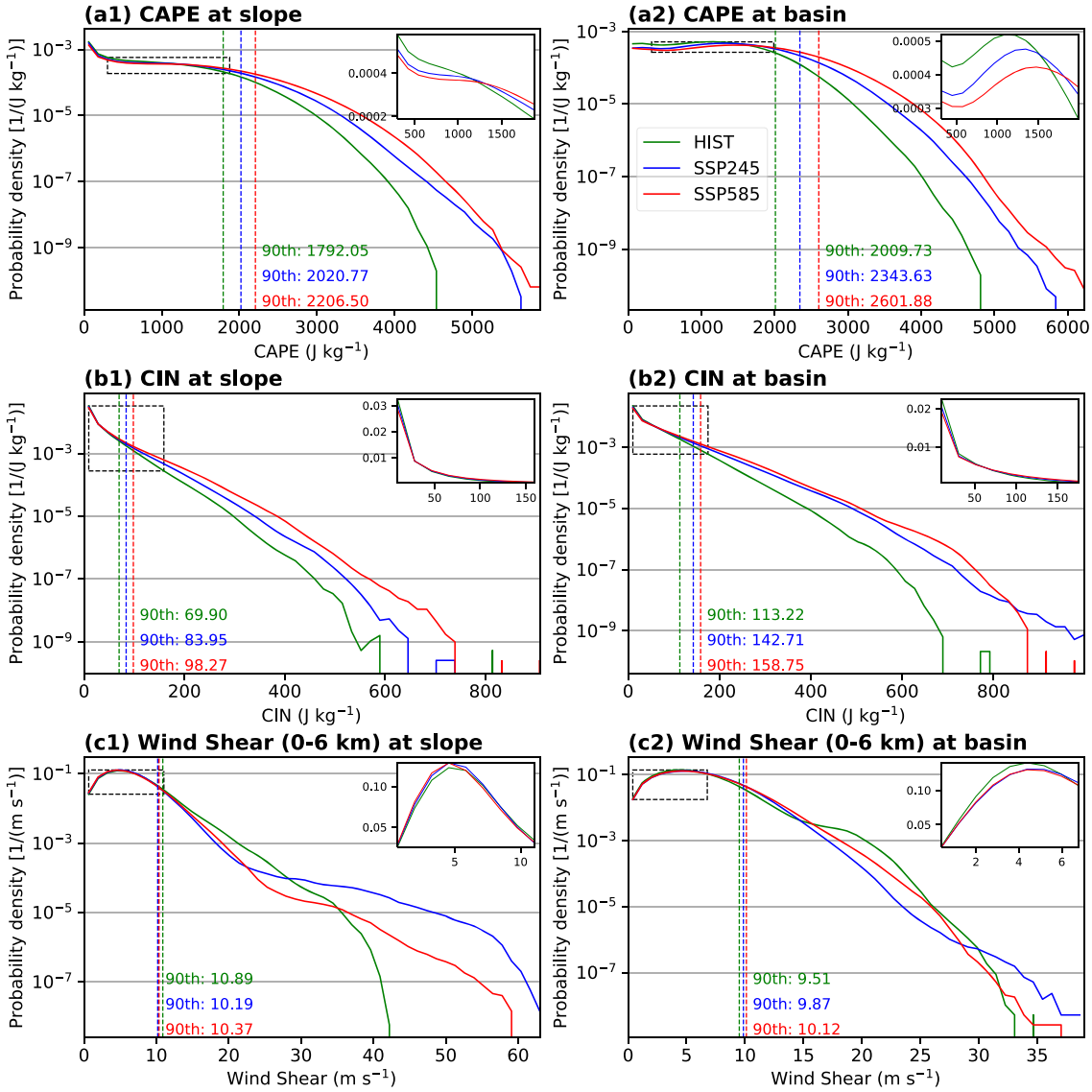

FIGURE 10 Probability density functions (PDFs) of (a1,a2) CAPE, (b1,b2) CIN, and (c1,c2) 0–6 km bulk wind-shear magnitude for HIST (green), SSP245 (blue), and SSP585 (red) during DJF at MCS genesis hotspots: (a1–c1) along the eastern slope of the Andes and (a2–c2) over the western Amazon Basin, as indicated by the blue rectangles in Figure 5. The subfigure in each panel represents the region marked by the black dashed box and features a *y*-axis with a linear scale. Vertical dashed lines mark the 90th percentile values. The Kolmogorov–Smirnov test reveals that the differences in distributions among HIST, SSP245, and SSP585 are statistically significant at the 0.05 level. [Colour figure can be viewed at wileyonlinelibrary.com]

organized MCSs (e.g., squall lines and bow echoes, Schumacher & Rasmussen, 2020). However, the role of vertical wind shear in convective systems is complex and can vary among different types of storms. Stronger wind shear is not always more conducive to the development of convective storms. For example, the optimal counteraction between cold pools and wind shear is more important to long-lived quasi-linear convective systems than the magnitude of wind shear itself (Huang *et al.*, 2019b; Rotunno *et al.*, 1988). This complexity is also illustrated by the PDFs of the 0–6 km bulk wind shear shown in Figure 10c1,c2. There are notable differences in the frequency of large wind-shear values among HIST, SSP245, and SSP585, but these differences are not systematically consistent. Specifically, there is a higher frequency of wind-shear values around 20 m·s^{-1} in HIST compared with SSP245 and SSP585, while wind-shear values greater than ~35 m·s^{-1} are more frequent in SSP245 and SSP585 than in HIST (Figure 10c1,c2). However, these patterns are not consistent in the PDFs of 0–1 km and 0–3 km bulk wind shears (not shown). Due to the complex roles of wind shear in convective systems, it is challenging to determine how these differences influence the organization and lifetime of MCSs, particularly given that MCS types are not distinguished in this study. Therefore, further examination is needed to understand how various types of MCSs change

under different climate scenarios. However, this analysis is beyond the scope of the current study and can be addressed in future research that focuses on wind shear and convection type.

Overall, these apparent changes in thermodynamic conditions, characterized by increased average values of CAPE, PW, and CIN, as well as a higher frequency of large CAPE and CIN values, foster an environment conducive to more intense convective precipitation, the formation and intensification of heavy precipitation-producing MCSs, and the suppression of weak precipitation in future warming scenarios. This trend is consistent with the findings in North America (Rasmussen *et al.*, 2020), which report a similar shift in convection population due to increased CAPE and CIN in a warming climate. Such an environmental thermodynamic condition change indicates a tendency to suppress weak convective activity, while concurrently creating a high-CAPE environment for more intense convection. These results emphasize the complex synergy of dynamic and thermodynamic forces in shaping future precipitation patterns, highlighting the vital importance of high-resolution CPM climate modeling for projecting regional hydroclimatic impacts.

4 | CONCLUSIONS AND DISCUSSION

To explore the potential impacts of climate change on precipitation and MCS characteristics in the Peruvian Central Andes region, this study conducts two future regional climate simulations at a convection-permitting grid spacing, where the WRF model is driven by a bias-corrected global dataset derived from the CMIP6 multi-model ensemble under the Shared Socioeconomic Pathways scenarios SSP2-4.5 and SSP5-8.5, corresponding to intermediate greenhouse gas emission and very high greenhouse gas emission scenarios. The simulations cover 11 years from 2070–2080 and adopt two nested domains with grid spacings of 15 and 3 km, covering the entire South America and the Peruvian Central Andes, respectively. The future simulations are compared with a historical simulation over a recent six-year period (2014–2019), which is driven by ERA5 reanalysis data as described in Huang *et al.* (2023a). Employing the same model configurations across the historical and future simulations facilitates a direct comparison, enabling a detailed analysis of climate change's potential effects on precipitation and MCSs in the Peruvian Central Andes. The key findings are outlined as follows.

(1) Changes in annual precipitation are geographic location dependent, while there is a consistent increase in the frequency of intense hourly precipitation across all regions examined, including both humid and arid areas, in a warming climate. There is a general decrease in annual precipitation over the western Amazon Basin, while an increase exists along the west coast below 1-km elevation and on the east slope of the Andes above 1 km, under both SSP2-4.5 and SSP5-8.5 emission scenarios, in comparison with the current climate. Annual precipitation differences between the two future scenarios are marginal across most regions. However, hourly precipitation contrasts become more pronounced, with precipitation intensity increasing by up to 10.2% at the 99.9th percentile under the SSP5-8.5 scenario compared with the SSP2-4.5 scenario.
(2) The future climate simulations under warming scenarios indicate a general increase in various aspects of MCS characteristics to the east of the Andes, including a higher frequency of MCS genesis, an enhancement in MCS precipitation intensity by up to ~10%, and an enlargement in MCS size that can exceed 10%, marking a significant shift from the historical simulation patterns.
(3) In future warming scenarios, synoptic-scale low-level jets are projected to strengthen, while variations in the low-level divergence field dominate the changes in annual precipitation, especially in that the weakened convergence over the western Amazon Basin reduces the annual precipitation there. The thermodynamic conditions in future warming scenarios are characterized by increased average values of CAPE, PW, and CIN, as well as a higher frequency of large CAPE and CIN values. Such changes shift the convection population, by suppressing weak convection while fostering a more unstable and moisture-rich atmosphere conducive to more intense convection and the formation and intensification of heavy precipitation-producing MCSs.

The changes in annual precipitation from the CPM projections are generally consistent with the CMIP6 multi-model ensemble mean projections (Almazroui *et al.*, 2021; Du *et al.*, 2022), which indicate an increase in future annual precipitation over the Peruvian Central Andes and a decrease over the Amazon Basin under SSP2-4.5 and SSP5-8.5 scenarios. This consistency is likely because the future simulations in this study are driven by the bias-corrected global dataset derived from the CMIP6 multi-model ensemble, although the CPM projections provide more detailed patterns due to their higher spatial resolution. The changes in hourly precipitation in the Peruvian Central Andes region are similar to previous CPM studies in other regions, such as the Contiguous United States (CONUS: (Prein *et al.*, 2017b)) and Central Europe (Knist *et al.*, 2020; Vanden Broucke *et al.*, 2019),

which also project an increase in the frequency and intensity of intense hourly precipitation under higher greenhouse gas emission scenarios. The projected overall increase in the frequency, precipitation intensity, and size of MCSs east of the Andes is also found in CPM studies in other regions, such as the CONUS (Haberlie *et al.*, 2023; Hwang *et al.*, 2023; Prein *et al.*, 2017a) and the West African Sahel (Fitzpatrick *et al.*, 2020). These changes can be explained by the changes in the thermodynamic environment, including CAPE, CIN (Prein *et al.*, 2017a; Rasmussen *et al.*, 2020; Schumacher & Rasmussen, 2020), and PW (Fitzpatrick *et al.*, 2020; Hwang *et al.*, 2023; Rasmussen *et al.*, 2020). Vertical wind shear is a crucial factor in MCS organization and development. However, Prein *et al.* (2017a) indicated that changes in wind shear are small and have minor effects on the changes in MCS dynamics in the CONUS according to their CPM projections. This is likely because they applied the pseudo global warming (PGW) approach in their future simulations (Liu *et al.*, 2017), which does not consider systematic changes in large-scale circulation. In this study, changes in wind-shear magnitude are seen. However, the organization and maintenance of MCSs are more influenced by how vertical wind shear interacts with convective updrafts and cold pools, rather than the magnitude of wind shear alone (Rotunno *et al.*, 1988; Schumacher & Rasmussen, 2020). Therefore, determining how changes in wind shear influence the organization and maintenance of MCSs is challenging, especially since different types of MCSs are not distinguished in this study. A detailed investigation into the role of wind shear in MCSs is beyond the scope of this study; future research on this topic is needed.

In summary, this study reveals a marked trend in precipitation and MCS activities in the Peruvian Central Andes region under a warming climate: an increase in the frequency of intense hourly precipitation and organized convective storms, coupled with a reduction in weak convective precipitation events. This shift indicates a heightened risk of flash flooding and landslides in this region in the future. The impacts of climate change in this study are shown to be a result of the complex synergy of dynamic and thermodynamic processes as well as interactions with terrain. This complexity underscores the necessity for high-resolution climate modeling to represent regional climate dynamics and local geographical features accurately. The findings not only highlight the value of convection-permitting climate simulations in understanding the hydroclimatic impacts of climate change and projecting future severe weather hazards, particularly in regions with complex terrain such as the Peruvian Central Andes, but also provide critical inputs for developing tailored climate mitigation and adaptation strategies in this region. It should be noted that constraints in computing resources have limited the simulation periods and the range of future climate scenarios in this study; thereby more long-term CPM simulations, such as the 22-year 4-km climate simulations over South America conducted by SAAG (Dominguez *et al.*, 2024; Liu *et al.*, 2022), and the inclusion of a broader range of climate-change scenarios are needed to confirm and strengthen the findings in this study. Ensembles of simulations using different model configurations are also desirable, to allow for the assessment of model and projection uncertainties.

AFFILIATIONS

[1]Center for Analysis and Prediction of Storms, University of Oklahoma, Norman, Oklahoma, USA

[2]School of Meteorology, University of Oklahoma, Norman, Oklahoma, USA

[3]South Central Climate Adaptation Science Center, University of Oklahoma, Norman, Oklahoma, USA

[4]Universidad Nacional de San Agustín de Arequipa, Arequipa, Peru

[5]Department of Geography and Environmental Sustainability, University of Oklahoma, Norman, Oklahoma, USA

[6]NSF National Center for Atmospheric Research, Boulder, Colorado, USA

[7]School of Civil Engineering and Environmental Engineering, University of Oklahoma, Norman, Oklahoma, USA

[8]Servicio Nacional de Meteorología e Hidrología del Perú (SENAMHI), Arequipa, Peru

ACKNOWLEDGMENTS

This project was primarily supported by grant No. 20163646499 from the Universidad Nacional de San Agustín de Arequipa (UNSA) of Peru through the IREES/LASI Global Change and Human Health Institute. Supplementary funding was provided by the Weathernews Chair funds. Yongjie Huang is partially supported by the U.S. Department of Energy's Atmospheric System Research, an Office of Science Biological and Environmental Research program, under DE-SC0024317. The authors acknowledge the Texas Advanced Computing Center (TACC) at the University of Texas at Austin (http://www.tacc.utexas.edu) for providing HPC resources through XSEDE allocation TG-ATM160014, which were used for the simulations. The authors also acknowledge high-performance computing support from Cheyenne (https://doi.org/10.5065/D6RX99HX) provided by NCAR's Computational and Information Systems Laboratory. NCAR is sponsored by the National Science Foundation. Some data processing was performed at the University of Oklahoma (OU) Supercomputing Center for Education and Research (OSCER).

CONFLICT OF INTEREST STATEMENT

All co-authors have declared that they do not have any competing interests.

DATA AVAILABILITY STATEMENT

The bias-corrected CMIP6 global dataset for dynamical downscaling is available at https://doi.org/10.11922/sciencedb.00487 (last access: December 15, 2021). The model outputs are too large to be publicly archived. Please contact the corresponding author for more information.

ORCID

Yongjie Huang https://orcid.org/0000-0001-7883-8768
Ming Xue https://orcid.org/0000-0003-1976-3238

REFERENCES

Almazroui, M., Ashfaq, M., Islam, M.N., Rashid, I.U., Kamil, S., Abid, M.A. et al. (2021) Assessment of CMIP6 performance and projected temperature and precipitation changes over South America. *Earth Systems and Environment*, 5, 155–183.

Anselmo, E.M., Machado, L.A., Schumacher, C. & Kiladis, G.N. (2021) Amazonian mesoscale convective systems: Life cycle and propagation characteristics. *International Journal of Climatology*, 41, 3968–3981.

Ascott, M., Christelis, V., Lapworth, D., Macdonald, D., Tindimugaya, C., Iragena, A. et al. (2023) On the application of rainfall projections from a convection-permitting climate model to lumped catchment models. *Journal of Hydrology*, 617, 129097.

Berthou, S., Kendon, E., Rowell, D., Roberts, M., Tucker, S. & Stratton, R. (2019) Larger future intensification of rainfall in the west african sahel in a convection-permitting model. *Geophysical Research Letters*, 46, 13299–13307.

Berthou, S., Kendon, E.J., Chan, S.C., Ban, N., Leutwyler, D., Schär, C. et al. (2020) Pan-European climate at convection-permitting scale: a model intercomparison study. *Climate Dynamics*, 55, 35–59.

Chang, R., Yan, Y., Wu, J., Wang, Y. & Gao, X. (2023) Projected PV plants in China's Gobi deserts would result in lower evaporation and wind. *Solar Energy*, 256, 140–150.

Chen, Y., Paschalis, A., Kendon, E., Kim, D. & Onof, C. (2021) Changing spatial structure of summer heavy rainfall, using convection-permitting ensemble. *Geophysical Research Letters*, 48, e2020GL090903.

Dominguez, F., Rasmussen, R., Liu, C., Ikeda, K., Prein, A., Varble, A. et al. (2024) Advancing South American water and climate science through multi-decadal convection-permitting modeling. *Bulletin of the American Meteorological Society*, 105, E32–E44.

Du, Y., Wang, D., Zhu, J., Wang, D., Qi, X. & Cai, J. (2022) Comprehensive assessment of CMIP5 and CMIP6 models in simulating and projecting precipitation over the global land. *International Journal of Climatology*, 42, 6859–6875.

Ek, M., Mitchell, K., Lin, Y., Rogers, E., Grunmann, P., Koren, V. et al. (2003) Implementation of Noah land surface model advances in the national centers for environmental prediction operational mesoscale eta model. *Journal of Geophysical Research: Atmospheres*, 108, 8851.

Feng, Z., Leung, L.R., Liu, N., Wang, J., Houze, R.A., Jr., Li, J. et al. (2021) A global high-resolution mesoscale convective system database using satellite-derived cloud tops, surface precipitation, and tracking. *Journal of Geophysical Research: Atmospheres*, 126, e2020JD034202.

Fitzpatrick, R.G., Parker, D.J., Marsham, J.H., Rowell, D.P., Guichard, F.M., Taylor, C.M. et al. (2020) What drives the intensification of mesoscale convective systems over the west African Sahel under climate change? *Journal of Climate*, 33, 3151–3172.

Fumière, Q., Déqué, M., Nuissier, O., Somot, S., Alias, A., Caillaud, C. et al. (2020) Extreme rainfall in Mediterranean France during the fall: added value of the CNRM-AROME convection-permitting regional climate model. *Climate Dynamics*, 55, 77–91.

Gensini, V.A., Haberlie, A.M. & Ashley, W.S. (2023) Convection-permitting simulations of historical and possible future climate over the contiguous united states. *Climate Dynamics*, 60, 109–126.

Giorgi, F. (2019) Thirty years of regional climate modeling: where are we and where are we going next? *Journal of Geophysical Research: Atmospheres*, 124, 5696–5723.

Guo, Z., Fang, J., Sun, X., Tang, J., Yang, Y. & Tang, J. (2020) Decadal long convection-permitting regional climate simulations over eastern china: evaluation of diurnal cycle of precipitation. *Climate Dynamics*, 54, 1329–1349.

Gutierrez, R.A., Junquas, C., Armijos, E., Sörensson, A.A. & Espinoza, J.-C. (2024) Performance of regional climate model precipitation simulations over the terrain-complex Andes-amazon transition region. *Journal of Geophysical Research: Atmospheres*, 129, e2023JD038618.

Haberlie, A.M., Ashley, W.S., Gensini, V.A. & Michaelis, A.C. (2023) The ratio of mesoscale convective system precipitation to total precipitation increases in future climate change scenarios. *npj Climate and Atmospheric Science*, 6, 150.

Halladay, K., Kahana, R., Johnson, B., Still, C., Fosser, G. & Alves, L. (2023) Convection-permitting climate simulations for South America with the met office unified model. *Climate Dynamics*, 61, 5247–5269.

Heikenfeld, M., Marinescu, P.J., Christensen, M., Watson-Parris, D., Senf, F., van den Heever, S.C. et al. (2019) tobac 1.2: towards a flexible framework for tracking and analysis of clouds in diverse datasets. *Geoscientific Model Development*, 12, 4551–4570.

Hersbach, H., Bell, B., Berrisford, P., Hirahara, S., Horányi, A., Muñoz-Sabater, J. et al. (2020) The era5 global reanalysis. *Quarterly Journal of the Royal Meteorological Society*, 146, 1999–2049.

Hodnebrog, Ø., Steensen, B., Marelle, L., Alterskjaer, K., Dalsøren, S. & Myhre, G. (2021) Understanding model diversity in future precipitation projections for South America. *Climate Dynamics*, 58, 1329–1347.

Hu, H., Leung, L.R. & Feng, Z. (2021) Early warm-season mesoscale convective systems dominate soil moisture–precipitation feedback for summer rainfall in central united states. *Proceedings of the National Academy of Sciences*, 118, e2105260118.

Huang, Y., Liu, Y., Liu, Y. & Knievel, J.C. (2019a) Budget analyses of a record-breaking rainfall event in the coastal metropolitan city of Guangzhou, China. *Journal of Geophysical Research: Atmospheres*, 124, 9391–9406.

Huang, Y., Liu, Y., Liu, Y., Li, H. & Knievel, J.C. (2019b) Mechanisms for a record-breaking rainfall in the coastal metropolitan city of Guangzhou, China: Observation analysis and nested very large eddy simulation with the WRF model. *Journal of Geophysical Research: Atmospheres*, 124, 1370–1391.

Huang, Y., Xue, M., Hu, X.-M., Martin, E., Novoa, H.M., McPherson, R.A. et al. (2023a) Characteristics of precipitation and mesoscale convective systems over the Peruvian Central Andes in multi 5-year convection-permitting simulations. *ESS Open*

Archive. Available from: https://https://doi.org/10.22541/essoar.170000370.07634797/v1

Huang, Y., Xue, M., Hu, X.-M., Martin, E., Novoa, H.M., McPherson, R.A. et al. (2023b) Convection-permitting simulations of precipitation over the Peruvian Central Andes: Strong sensitivity to planetary boundary layer parameterization. *Journal of Hydrometeorology*, 24, 1969–1990.

Hwang, Y., Zhao, X., You, C.-H. & Li, Y. (2023) Climatological features of future MCSS in convection-permitting climate models using CMIP6 and ERA5 in the central united states. *Quarterly Journal of the Royal Meteorological Society*, 149, 3135–3163.

Iacono, M.J., Delamere, J.S., Mlawer, E.J., Shephard, M.W., Clough, S.A. & Collins, W.D. (2008) Radiative forcing by long-lived greenhouse gases: Calculations with the AER radiative transfer models. *Journal of Geophysical Research: Atmospheres*, 113, D13103.

Ikeda, K., Rasmussen, R., Liu, C., Newman, A., Chen, F., Barlage, M. et al. (2021) Snowfall and snowpack in the western us as captured by convection permitting climate simulations: current climate and pseudo global warming future climate. *Climate Dynamics*, 57, 2191–2215.

IPCC. (2021) *Climate Change 2021 - The Physical Science Basis: Working Group I Contribution to the Sixth Assessment Report of the Intergovernmental Panel on Climate Change*, 1st edition. Cambridge, United Kingdom and New York, NY, USA: Cambridge University Press.

IPCC. (2022a) *Climate Change 2022 - Impacts, Adaptation and Vulnerability: Working Group II Contribution to the Sixth Assessment Report of the Intergovernmental Panel on Climate Change*, 1st edition. Cambridge, United Kingdom and New York, NY, USA: Cambridge University Press.

Jiménez, P.A., Dudhia, J., González-Rouco, J.F., Navarro, J., Montávez, J.P. & García-Bustamante, E. (2012) A revised scheme for the WRF surface layer formulation. *Monthly Weather Review*, 140, 898–918.

Jones, C., Mu, Y., Carvalho, L.M. & Ding, Q. (2023) The south America low-level jet: form, variability and large-scale forcings. *npj Climate and Atmospheric Science*, 6, 175.

Juckes, M., Taylor, K.E., Durack, P.J., Lawrence, B., Mizielinski, M.S., Pamment, A. et al. (2020) The CMIP6 data request (DREQ, version 01.00. 31). *Geoscientific Model Development*, 13, 201–224.

Karki, R., Gerlitz, L., Schickhoff, U., Scholten, T., Böhner, J. et al. (2017) Quantifying the added value of convection-permitting climate simulations in complex terrain: a systematic evaluation of WRF over the Himalayas. *Earth System Dynamics*, 8, 507–528.

Kendon, E., Prein, A., Senior, C. & Stirling, A. (2021) Challenges and outlook for convection-permitting climate modelling. *Philosophical Transactions of the Royal Society A*, 379, 20190547.

Kendon, E.J., Stratton, R.A., Tucker, S., Marsham, J.H., Berthou, S., Rowell, D.P. et al. (2019) Enhanced future changes in wet and dry extremes over Africa at convection-permitting scale. *Nature Communications*, 10, 1794.

Knist, S., Goergen, K. & Simmer, C. (2020) Evaluation and projected changes of precipitation statistics in convection-permitting WRF climate simulations over Central Europe. *Climate Dynamics*, 55, 325–341.

Kouadio, K., Bastin, S., Konare, A. & Ajayi, V.O. (2020) Does convection-permitting simulate better rainfall distribution and extreme over Guinean coast and surroundings? *Climate Dynamics*, 55, 153–174.

Kukulies, J., Chen, D. & Curio, J. (2021) The role of mesoscale convective systems in precipitation in the Tibetan plateau region. *Journal of Geophysical Research: Atmospheres*, 126, e2021JD035279.

Li, P., Furtado, K., Zhou, T., Chen, H. & Li, J. (2021) Convection-permitting modelling improves simulated precipitation over the central and eastern tibetan plateau. *Quarterly Journal of the Royal Meteorological Society*, 147, 341–362.

Li, P., Moseley, C., Prein, A.F., Chen, H., Li, J., Furtado, K. et al. (2020) Mesoscale convective system precipitation characteristics over East Asia. Part I: Regional differences and seasonal variations. *Journal of Climate*, 33, 9271–9286.

Lind, P., Belušić, D., Christensen, O.B., Dobler, A., Kjellström, E., Landgren, O. et al. (2020) Benefits and added value of convection-permitting climate modeling over Fenno-Scandinavia. *Climate Dynamics*, 55, 1893–1912.

Lind, P., Belušić, D., Médus, E., Dobler, A., Pedersen, R.A., Wang, F. et al. (2023) Climate change information over Fenno-Scandinavia produced with a convection-permitting climate model. *Climate Dynamics*, 61, 519–541.

Liu, C., Ikeda, K., Rasmussen, R., Barlage, M., Newman, A.J., Prein, A.F. et al. (2017) Continental-scale convection-permitting modeling of the current and future climate of North America. *Climate Dynamics*, 49, 71–95.

Liu, C., Ikeda, K., Rasmussen, R., Dominguez, F., Prein, A.F., Dudhia, J. et al. (2022) An overview of two-decade-long convection permitting regional climate downscaling over the continental South America. In: *American Geophysical Union Fall Meeting*. Chicago, IL: American Geophysical Union. Available from: https://agu.confex.com/agu/fm22/meetingapp.cgi/Paper/1115319

Lucas-Picher, P., Argüeso, D., Brisson, E., Tramblay, Y., Berg, P., Lemonsu, A. et al. (2021) Convection-permitting modeling with regional climate models: Latest developments and next steps. *Wiley Interdisciplinary Reviews: Climate Change*, 12, e731.

Marengo, J.A., Douglas, M.W. & Silva Dias, P.L. (2002) The south American low-level jet east of the Andes during the 1999 LBA-TRMM and LBA-wet AMC campaign. *Journal of Geophysical Research: Atmospheres*, 107, LBA–47.

Marengo, J.A., Soares, W.R., Saulo, C. & Nicolini, M. (2004) Climatology of the low-level jet east of the Andes as derived from the NCEP–NCAR reanalyses: Characteristics and temporal variability. *Journal of Climate*, 17, 2261–2280.

Nakanishi, M. & Niino, H. (2009) Development of an improved turbulence closure model for the atmospheric boundary layer. *Journal of the Meteorological Society of Japan Ser. II*, 87, 895–912.

O'Neill, B.C., Tebaldi, C., van Vuuren, D.P., Eyring, V., Friedlingstein, P., Hurtt, G. et al. (2016) The scenario model intercomparison project (scenariomip) for CMIP6. *Geoscientific Model Development*, 9, 3461–3482.

Pabón-Caicedo, J.D., Arias, P.A., Carril, A.F., Espinoza, J.C., Borrel, L.F., Goubanova, K. et al. (2020) Observed and projected hydroclimate changes in the Andes. *Frontiers in Earth Science*, 8, 61.

Paccini, L. & Stevens, B. (2023) Assessing precipitation over the Amazon basin as simulated by a storm-resolving model. *Journal of Geophysical Research: Atmospheres*, 128, e2022JD037436.

Potter, E.R., Fyffe, C.L., Orr, A., Quincey, D.J., Ross, A.N., Rangecroft, S. et al. (2023) A future of extreme precipitation and droughts in the Peruvian Andes. *npj Climate and Atmospheric Science*, 6, 96.

Prein, A.F., Langhans, W., Fosser, G., Ferrone, A., Ban, N., Goergen, K. et al. (2015) A review on regional convection-permitting climate modeling: Demonstrations, prospects, and challenges. *Reviews of Geophysics*, 53, 323–361.

Prein, A.F., Liu, C., Ikeda, K., Bullock, R., Rasmussen, R.M., Holland, G.J. et al. (2020) Simulating North American mesoscale convective systems with a convection-permitting climate model. *Climate Dynamics*, 55, 95–110.

Prein, A.F., Liu, C., Ikeda, K., Trier, S.B., Rasmussen, R.M., Holland, G.J. et al. (2017a) Increased rainfall volume from future convective storms in the US. *Nature Climate Change*, 7, 880–884.

Prein, A.F., Rasmussen, R.M., Ikeda, K., Liu, C., Clark, M.P. & Holland, G.J. (2017b) The future intensification of hourly precipitation extremes. *Nature Climate Change*, 7, 48–52.

Qing, Y. & Wang, S. (2021) Multi-decadal convection-permitting climate projections for china's greater bay area and surroundings. *Climate Dynamics*, 57, 415–434.

Rasmussen, K.L., Prein, A.F., Rasmussen, R.M., Ikeda, K. & Liu, C. (2020) Changes in the convective population and thermodynamic environments in convection-permitting regional climate simulations over the United States. *Climate Dynamics*, 55, 383–408.

Roca, R. & Fiolleau, T. (2020) Extreme precipitation in the tropics is closely associated with long-lived convective systems. *Communications Earth & Environment*, 1, 18.

Rosales, A.G., Junquas, C., da Rocha, R.P., Condom, T. & Espinoza, J.-C. (2022) Valley–mountain circulation associated with the diurnal cycle of precipitation in the tropical Andes (Santa River Basin, Peru). *Atmosphere*, 13, 344.

Rotunno, R., Klemp, J.B. & Weisman, M.L. (1988) A theory for strong, long-lived squall lines. *Journal of Atmospheric Sciences*, 45, 463–485.

Salio, P., Nicolini, M. & Zipser, E.J. (2007) Mesoscale convective systems over southeastern south America and their relationship with the south American low-level jet. *Monthly Weather Review*, 135, 1290–1309.

Schumacher, R.S. & Rasmussen, K.L. (2020) The formation, character and changing nature of mesoscale convective systems. *Nature Reviews Earth and Environment*, 1, 300–314.

Schumacher, V., Fernández, A., Justino, F. & Comin, A. (2020) WRF high resolution dynamical downscaling of precipitation for the central Andes of Chile and Argentina. *Frontiers in Earth Science*, 8, 328.

Skamarock, W.C., Klemp, J.B., Dudhia, J., Gill, D.O., Liu, Z., Berner, J. et al. (2019) *A description of the advanced research wrf model version 4*. National Center for Atmospheric Research: Boulder, CO, USA, p. 145.

Stratton, R.A., Senior, C.A., Vosper, S.B., Folwell, S.S., Boutle, I.A., Earnshaw, P.D. et al. (2018) A pan-African convection-permitting regional climate simulation with the met office unified model: Cp4-Africa. *Journal of Climate*, 31, 3485–3508.

Sulca, J.C. & da Rocha, R.P. (2021) Influence of the coupling south Atlantic convergence zone-el niño-southern oscillation (SACZ-ENSO) on the projected precipitation changes over the central Andes. *Climate*, 9, 77.

Sun, X., Xue, M., Brotzge, J., McPherson, R.A., Hu, X.-M. & Yang, X.-Q. (2016) An evaluation of dynamical downscaling of central plains summer precipitation using a WRF-based regional climate model at a convection-permitting 4 km resolution. *Journal of Geophysical Research: Atmospheres*, 121, 13–801.

Thompson, G., Field, P.R., Rasmussen, R.M. & Hall, W.D. (2008) Explicit forecasts of winter precipitation using an improved bulk microphysics scheme. Part II: Implementation of a new snow parameterization. *Monthly Weather Review*, 136, 5095–5115.

Tiedtke, M. (1989) A comprehensive mass flux scheme for cumulus parameterization in large-scale models. *Monthly Weather Review*, 117, 1779–1800.

Vanden Broucke, S., Wouters, H., Demuzere, M. & van Lipzig, N.P. (2019) The influence of convection-permitting regional climate modeling on future projections of extreme precipitation: dependency on topography and timescale. *Climate Dynamics*, 52, 5303–5324.

Vera, C., Baez, J., Douglas, M., Emmanuel, C., Marengo, J., Meitin, J. et al. (2006) The south American low-level jet experiment. *Bulletin of the American Meteorological Society*, 87, 63–78.

Wang, Y., Xiang, Y., Han, Z. & Song, L. (2023) Future extreme high-temperature risk in the Beijing-Tianjin-Hebei urban agglomeration of china based on a regional climate model coupled with urban parameterization scheme. *Theoretical and Applied Climatology*, 153, 621–634.

Wu, L. & Zheng, H. (2023) Regional climate effects of irrigation under central Asia warming by 2.0°c. *Remote Sensing*, 15, 3672.

Xu, Z., Han, Y., Tam, C.-Y., Yang, Z.-L. & Fu, C. (2021) Bias-corrected cmip6 global dataset for dynamical downscaling of the historical and future climate (1979–2100). *Scientific Data*, 8, 293.

Yang, X., Li, D., Yang, Z., Wu, K., Ji, L., Zhou, Z. et al. (2023) Revealing historical observations and future projections of precipitation over northwest china based on dynamic downscaled cmip6 simulations. *Frontiers in Earth Science*, 10, 1090221.

Zaitchik, B.F., Rodell, M., Biasutti, M. & Seneviratne, S.I. (2023) Wetting and drying trends under climate change. *Nature Water*, 1, 502–513.

Zhu, K., Xue, M., Zhou, B., Zhao, K., Sun, Z., Fu, P. et al. (2018) Evaluation of real-time convection-permitting precipitation forecasts in china during the 2013–2014 summer season. *Journal of Geophysical Research: Atmospheres*, 123, 1037–1064.

How to cite this article: Huang, Y., Xue, M., Hu, X.-M., Martin, E., Novoa, H.M., McPherson, R.A. *et al.* (2024) Increasing frequency and precipitation intensity of convective storms in the Peruvian Central Andes: Projections from convection-permitting regional climate simulations. *Quarterly Journal of the Royal Meteorological Society*, 1–20. Available from: https://doi.org/10.1002/qj.4820